NASA/CR— 1998— 207450

IN-92-CR
067987

# A Multiwavelength Study of Coronal Structure:

# A Simultaneous Observation from NIXT and YOHKOH

Grant NAGW-4644

Final Report

For The Period of Performance 04/01/95 Through 09/30/97

Principal Investigator:

Dr. Leon Golub

February 1998

The Smithsonian Astrophysical Observatory
is a member of the
Harvard-Smithsonian Center for Astrophysics
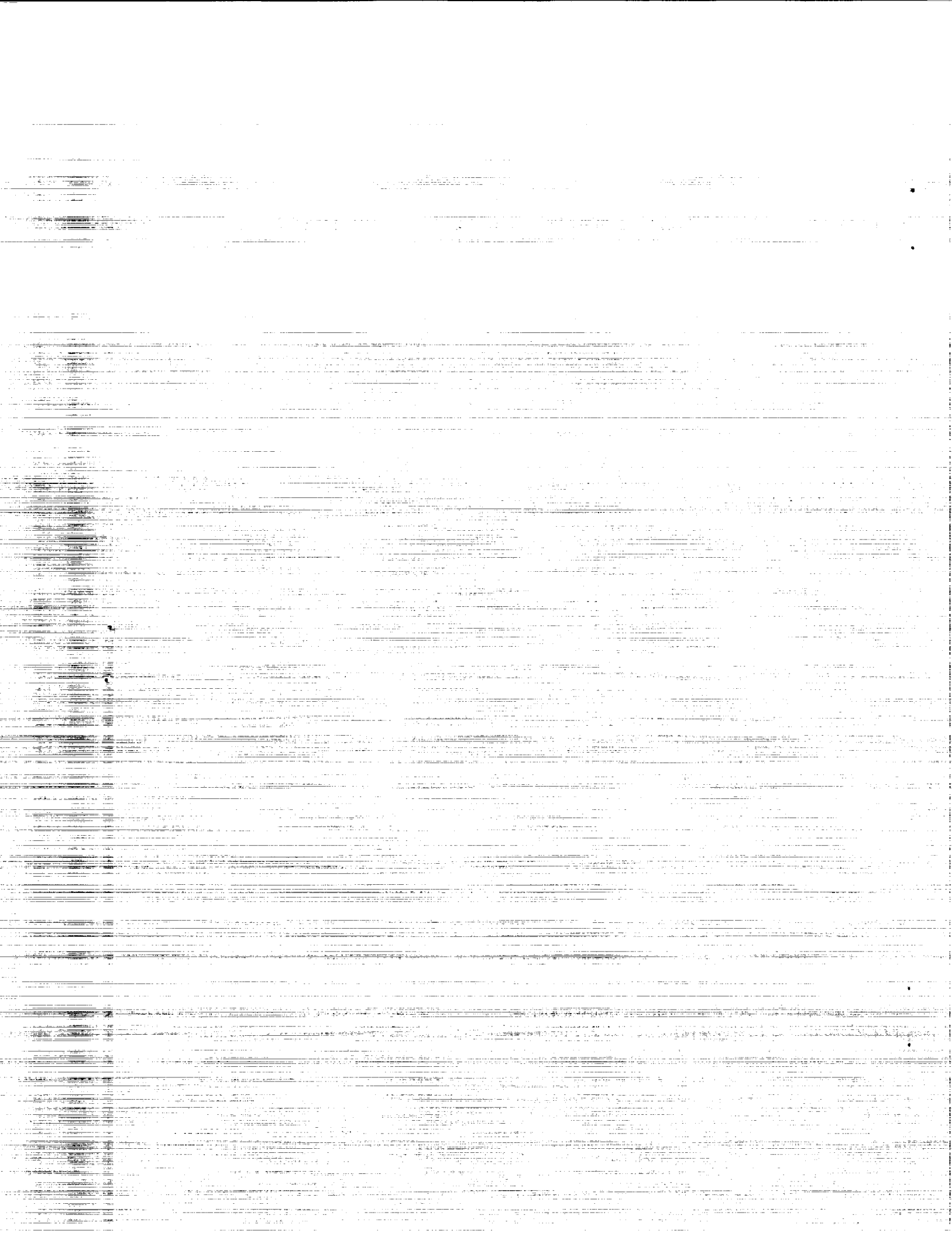
I. Work Completed During the Past Year:

During the past year this grant has funded research by Drs. Golub and DeLuca, graduate student A. Daw and undergraduates Ms. Wills and Mr. Hartl. The following is a brief summary of the published papers, abstracts and talks which have been supported by Grant NAGW-4644 within the present grant performance period.

1. The paper "Temperature Structure of the Solar Corona: Comparison of NIXT and Yohkoh X-ray Images" by T, Yoshida, S. Tsuneta, L. Golub, K. Strong and Y. Ogawara, has been published in PASJ. Solar soft x-ray images taken simultaneously by the Yohkoh SXT and the NIXT sounding rocket reveal significantly different coronal structures. Away from active regions, loops are generally seen in the SXT while footpoints are seen in the NIXT. The difference is due to the difference in the temperature responses of the telescopes: NIXT is sensitive in the range from 1 - 3 MK and SXT is sensitive at temperatures above 2.5 MK. The morphological differences reflect the multi-temperature nature of the solar plasma.

A copy of the paper is appended to this report. A follow-up study, comparing the NIXT and the SXT in active regions is under way. Preliminary results show that entire sets of loops, visible in one instrument are not sene in the other. The effect works in *both* directions.

2. The paper "NIXT X-Ray Bright Point Survey: Observation and Classification of Data from 12 April 1993," by M. J. Wills, M. D. Hartl, E. E. DeLuca, and L. Golub, has been brought to advanced draft form and is being readied for submission to Solar Physics. The aim of this study is to examine the morphology of x-ray bright points together with the nature of the underlying magnetic structure. In addition, due to the unprecedented number of XBPs visible in the 12 April 1993 NIXT photographs, we are able to determine excellent estimates for various parameters relevant to theoretical bright point models: the fraction of bright points with clear bipolar signatures, characteristic angular size, and emitted energy flux. Due to the large number of bright points in our study, we are also able to determine statistically significant XBP distributions by solar latitude. Simultaneous observations with the Yohkoh SXT are used to construct temperature and density distributions for the sample of XBP visible in both datasets.

3. The paper "Modeling Magnetic Flux Emergence", by M. Wills and E. DeLuca was presented at the Solar Physics Division/AAS meeting in Madison in June 1996.

4. "Difficulties in Observing Coronal Structure". This represents an invited keynote paper for the STEPWG1 Workshop, "Measurements and Analysis of Solar 3D Magnetic Fields. The printed version has appeared as a refereed publication in a special issue of Solar Physics, **174**, 99 (1997).

# Temperature Structure of the Solar Corona: Comparison of the NIXT and Yohkoh X-Ray Images

Tsuyoshi YOSHIDA and Saku TSUNETA
*Institute of Astronomy, The University of Tokyo, Mitaka, Tokyo 181*

Leon GOLUB
*Smithsonian Astrophysical Observatory, 60 Garden Street, Cambridge, MA 02138, USA*

Keith STRONG
*Lockheed Solar and Astrophysics Laboratory, 3251 Hanover Street, Palo Alto, CA 94304, USA*
and
Yoshiaki OGAWARA
*Institute of Space and Astronautical Science, Sagamihara, Kanagawa 229*

## Abstract

Solar soft X-ray images taken simultaneously by the Yohkoh and the Normal Incidence X-ray Telescope (NIXT) reveal significantly different coronal structures. Coronal loops are more clearly seen in the Yohkoh images, and the isolated island-like structures seen in the NIXT image have been found to correspond to the footpoints of the Yohkoh loops. The difference is due to the difference in the temperature response of the telescopes: NIXT is sensitive to temperatures ranging from 0.9 to 3 MK, while Yohkoh is more sensitive to temperatures above 2.5 MK. The morphological differences reflect the multi-temperature (1–5 MK) nature of the solar coronal plasmas.

**Key words:** Sun: corona — Sun: magnetic fields — Sun: X-rays — Sun: Yohkoh

## 1. Introduction

The soft X-ray telescope (Tsuneta et al. 1991) on Yohkoh (Ogawara et al. 1991) reveals various magnetic constituents of the solar corona, such as loops, cusps, and (unipolar) holes (Acton et al. 1992). The plasma temperatures of these structures have been obtained using pairs of broadband filters for flare loops (Tsuneta et al. 1992; McTiernan et al. 1993), transient brightenings (Shimizu et al. 1994; Shimizu 1995), steady coronal loops (Kano, Tsuneta 1994), and coronal holes and the quiet Sun (Hara et al. 1994). Figure 1 shows the temperature response of the Soft X-ray Telescope (SXT) aboard Yohkoh. The telescope is more sensitive to plasmas with temperatures above 2.5 MK. In other words, SXT may not be capable of seeing structure with lower-temperature plasmas, unless the emission measure at the low temperatures is sufficient to compensate for the turnoff below 2.5 MK. It may thus be misleading to assume that the Yohkoh Soft X-ray Telescope can see all of the magnetic structures in the solar corona.

This letter reports the first simultaneous observation of the X-ray corona by the SAO Normal Incidence X-ray Telescope (NIXT) aboard a sounding rocket (Golub, Herant 1989) and the SXT. The differences in the op-

tics used for the telescopes result in significant differences in the temperature response of the telescopes. Normal-incidence multilayer technology is utilized for NIXT. Thus, NIXT has a sensitivity in a narrow range of wavelengths, and is sensitive only to the lines and the continuum within its passband. NIXT has a wavelength passband centered at 63.5 Å with a width of 1.4 Å. The passband contains Mg X at 63.3 Å, and Fe XVI at 63.7 Å. The contribution functions of these lines have peaks at around 1.2 MK and 2.5 MK for Mg and Fe lines, respectively. The NIXT and SXT temperature response is shown in figure 1. [We used the spectral data of Mewe et al. (1985, 1986) to obtain the emissivity.]

The Yohkoh SXT, on the other hand, utilizes grazing-incidence optics, and is more sensitive to the temperatures above 2.5 MK (50% of the peak response of the thin aluminum filter in figure 1). NIXT responds to lower temperatures than does Yohkoh. Thus, taken together, the two instruments have the capability to see all of the magnetic structures in the temperature range from 0.9 to 10 MK. The key characteristics of the two telescopes are summarized in table 1.

In this letter we compare the images taken by the two telescopes and discuss the temperature structure of the solar corona.
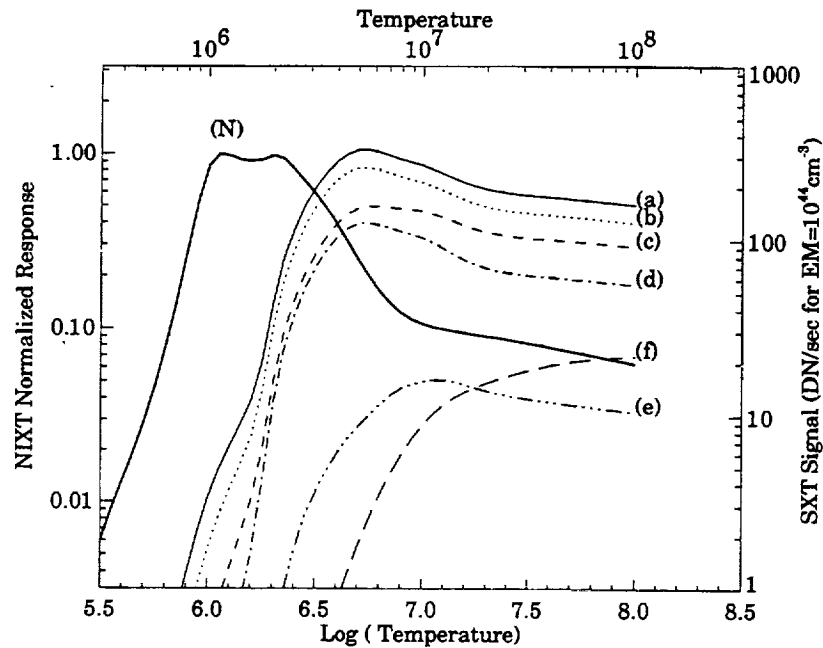
Fig. 1. (a–f) Temperature response of the Yohkoh SXT for various analysis filters: (a) open, (b) Al 1265 Å, (c) Al/Mg/Mn, (d) Mg 2.52 $\mu$m, (e) Al 11.6 $\mu$m, (f) Be 119 $\mu$m. (N) The normalized temperature response of NIXT. We used the spectral data of Mewe et al. (1985, 1986).

Table 1. Characteristics of the SXT and NIXT instruments.

| | SXT | NIXT |
|---|---|---|
| Optics ..................................... | Grazing incidence | Normal incidence multilayer |
| Sensitive temperature range ............... | Above 2.5 MK | 0.9–2 MK |
| | | 1.2 MK (Mg X) |
| | | 2.5 MK (Fe XVI) |
| Spatial resolution ......................... | $3''$ | $0''75$ |
| Detector ................................... | CCD | Film |

## 2. Observations

NIXT was successfully launched on 1993 April 12. NIXT observed the solar corona from UT 17:17 to 17:23, and simultaneous Yohkoh observations were successfully made. The NIXT experiment uses a film readout; the images were digitized to 4000 × 4000 pixel data with a pixel size of $0''6$. The image is then a 2 × 2 pixel summed; the image used in the present analysis had a pixel size of $1''2$. The pixel size of the Yohkoh whole-Sun images is $4''91$ (2 × 2 pixel sum). Alignment of the two images was carried out by using the solar limb as well as scattered X-ray bright points. The accuracy of the alignment was confirmed to be better than that of the SXT 2 × 2 summed pixel size ($4''91$) by examining the mutual lo-

cations of the solar limb and the X-ray bright points at various positions of the Sun.

### 2.1. X-Ray Morphology

Figure 2 (Plate 3) shows the NIXT and Yohkoh images of the whole Sun taken at around 17:13 UT on 1993 April 12. The two images appear to be quite different. We can notice numerous loop structures not only in active regions, but also in the quiet corona outside active regions in the Yohkoh image. In the NIXT image, on the other hand, loop structures are seen only in the active regions, and many island-like patchy structures are seen in the quiet regions.

A quiet region indicated as I in figure 2 (Plate 3) is

shown in figure 3 (Plate 3). It contains complex structures, many of which can be identified as coronal loops in the Yohkoh image [figure 3a (Plate 3)]. The NIXT image of the same quiet region [figure 3b (Plate 3)] does not show any significant structure corresponding to the Yohkoh loops. Figure 3c (Plate 3) shows the locations of the Yohkoh coronal loops on the NIXT image. The island-like structures are generally located at the footpoint portions of the Yohkoh loops. Exactly the same tendency is seen in the quiet Sun just south of the bright active region [figure 4 (Plate 4)]. [The region is indicated as II in figure 2. (Plate 3)] At the footpoint portions of the Yohkoh loops, there are generally compact structures in the NIXT image, as shown in figure 4c (Plate 4). This comparison also shows that the diameters of the NIXT footpoints are similar to those of the Yohkoh loops. The connectivity between the Yohkoh and NIXT structures is good, and the combined structures would show real coronal magnetic structures.

The active region is also shown in figure 4 (Plate 4). There are numerous loop structures within the active region in the NIXT image [figure 4b (Plate 4)] as well. They are seen only in the active region in the NIXT image. The coincidence of the SXT and NIXT loops in the active region appears at first glance to be good. A detailed comparison, however, implies that the NIXT loops appear to be different from the Yohkoh loops in both position and shape [figure 4c (Plate 4)]. For instance, the footpoint portions indicated as C in figure 4b (Plate 4) (NIXT image) appear to be sharper compared with the NIXT footpoints seen in the quiet sun. Such a significant footpoint structure is not seen in the Yohkoh image [figure 4a (Plate 4)].

### 2.2. Temperature Analysis

We derived the temperatures of the coronal structures using a pair of SXT broadband filters (Hara et al. 1992; Kano, Tsuneta 1994). We chose several regions for the temperature analysis; the regions indicated by boxes in figures 3 (Plate 3) and 4 (Plate 4) were analyzed. Regions B and E in figures 3 and 4 include the tops of loops, and the emission of the region is dominated by that of the tops of the loops. Regions A and F are located around the footpoint portions of the loop structures in the quiet Sun. Region D in figure 3 (Plate 3) is located around the top of the loops, and region C is at the footpoint portion of the loops. We can obtain the temperature of each footpoint region from the Yohkoh data, even if there is no corresponding structure in the Yohkoh image. This is because there is a sufficient number of photons in the footpoint regions of the Yohkoh image.

The SXT filters used in this analysis were thin-aluminum and Al/Mg/Mn composites (Tsuneta et al. 1991). The dark current was subtracted from the images.

Although the SXT images used in the analysis were taken 9 min apart in time, we confirmed that there had been no appreciable changes in the relevant coronal structures at that time. A temperature analysis of the bright active region [figure 4 (Plate 4)] was not performed, because the time separation of the two images with proper exposures for the active region was about 15 min, and the stability of the active region structure is unlikely to be over that length of time.

This combination of filters provides a good temperature diagnostic capability in the temperature range below 4 MK. We assume isothermality in each pixel and choose pixels with a sufficient number of photons to give a temperature error better than 0.3 MK. Figure 5 shows the derived temperature distribution of regions A through F, showing the number of pixels as a function of the temperature. The errors in the temperatures due to the Poisson noise of the incident photons are less than 0.3 MK. Figure 5 shows clear differences in the temperatures depending on the location. The temperatures of the areas dominated by the NIXT islands (regions A and F) are from 1 to 1.5 MK, whereas those dominated by the Yohkoh loops (regions B and E) are from 1.5 to 2.5 MK. The loop top region D has a temperature of 2 MK, and footpoint C has a temperature of 1.5 MK. The temperature difference ranged from 0.5 to 1 MK, which is statistically significant. Note that these temperatures were obtained from the Yohkoh data alone and that there was no allowance for a systematic error in the temperatures of the loop tops and the footpoints. Table 2 tabulates the peak temperatures of figure 5 and the nominal mean emission measures of the selected regions.

### 3. Discussion

We have so far demonstrated that the NIXT island-structures correspond to the footpoints of the SXT loops. There may be a possibility that the NIXT structures were (separate) low-lying cool loop structures. We can, however, rule out this possibility because the positional correspondence is generally excellent.

We have also shown that the the regions that contain the NIXT island-like structures in the quiet Sun have lower temperatures (1–1.5 MK) than the loops seen by Yohkoh (1.5–2 MK). The NIXT telescope is sensitive to lower temperatures, and tends preferentially to see the structures closer to the footpoints, whereas the Yohkoh telescope is more sensitive to higher temperatures and thus sees more coronal structures. This qualitatively explains the significant differences between the two images.

Since the NIXT temperature sensitivity is almost flat between 1 MK and 2 MK, as shown in figure 1, the emission measures of the coronal loops must be sufficiently low to make them invisible in the NIXT image. Table 2 indeed shows that the emission measures of the
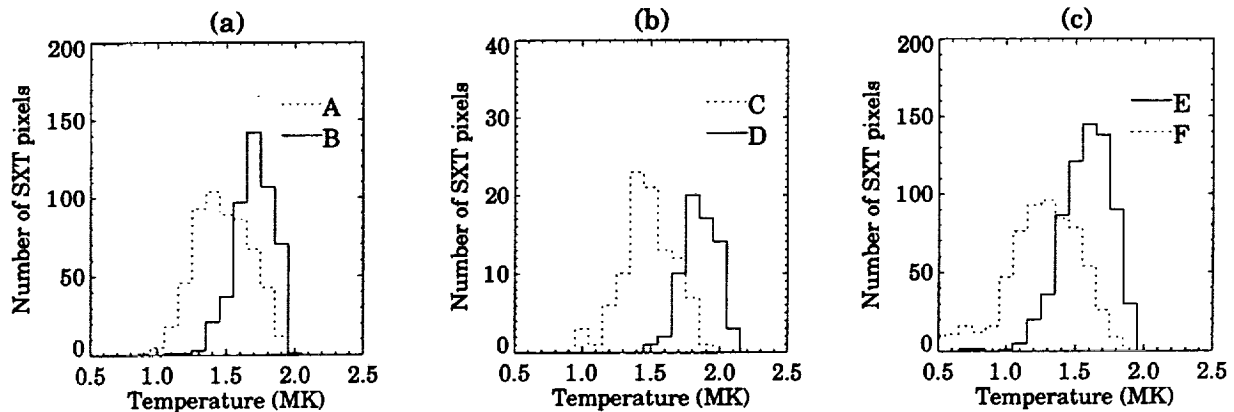
Fig. 5. Temperature distribution obtained with the Yohkoh data: Number of pixels as a function of the temperatures. The pixels which have statistical errors more than 0.3 MK owing to poor count statistics are not counted in the diagram. The locations of the distributions are shown in the figures 3 (Plate 3) and 4 (Plate 4). The temperatures of the footpoint portions are significantly lower than those of the upper loop structures.

Table 2. Peak temperature and mean emission measure.

| Region (indicated in figures 3 and 4) | Peak temperature (MK) | Mean emission measure ($10^{44}$ cm$^{-3}$) |
|---|---|---|
| A ............. | 1.4 | 11.0 ± 4.0 |
| B ............. | 1.7 | 2.9 ± 0.1 |
| C ............. | 1.4 | 4.8 ± 0.2 |
| D ............. | 1.8 | 3.8 ± 0.3 |
| E ............. | 1.6 | 3.8 ± 0.1 |
| F ............. | 1.3 | 14.0 ± 3.0 |

Note: The peak temperatures are derived from the histograms shown in figure 5. The histogram's temperature step is 0.1 MK. The mean emission measures are the average emission measures per one SXT pixel.

loop tops are a factor of 1.3–4.0 smaller than those of the footpoints. However, this is apparently not sufficient to quantitatively explain the differences of the two images. We conclude that there is a significantly greater emission measure around the footpoints with temperatures lower than the temperature deduced here from Yohkoh data: the SXT footpoint emission measure must be regarded as being the lower limits, because of its poor sensitivity in the temperature range.

We can also consider the NIXT spectral response as the cause of the discrepancy: NIXT observes mainly lines, mostly Mg X and Fe XVI. The NIXT temperature response may, thus, be sensitive to the relevant atomic parameters assumed in the spectral code. Indeed, Golub and Herant (1989) obtained a significantly different re-

sponse on the basis of the different spectral code. Their sensitivity at 1.2 MK is about a factor of 3 higher than that at 3 MK, whereas the sensitivity is almost flat over the temperature range from 1 to 2 MK in figure 1. The ratio between 1 MK (footpoint) and 2 MK (loop top) is about 5 in Golub and Herant (1989). If the ratio is combined with the difference of the emission measure, the resultant intensity difference between the loop tops and the foot points may reach a factor of 10. This would also contribute to the significant differences of the two images.

The observation indicates that the temperatures of the coronal structures become lower as we go lower in the corona, and that below a certain height the structures become invisible to Yohkoh. This result is consistent with an analysis of the temperature distribution along the coronal loops (Kano, Tsuneta 1994).

The situation of the active region is less clear. If the NIXT loops in the active region have temperatures as high as 3–4 MK, they should have been seen in the Yohkoh images. Thus, there is a possibility that the NIXT loops in the active region have temperatures that are invisible to Yohkoh (as low as 1 MK). The temperatures of some active-region loops can reach 2–6 MK, as seen from the Yohkoh data (Hara et al. 1992; Kano, Tsuneta 1994). The combined NIXT and Yohkoh data sets imply that high-temperature loops are located in close proximity to low-temperature loops in the active region.

Although the sensitivity of the Yohkoh telescope to temperatures below 2.5 MK is reduced, as shown in figure 1, the temperatures derived here for the footpoints are about 1–1.5 MK. These are among the lowest temper-

atures so far obtained by a Yohkoh temperature analysis. The analysis suggests that we may be able to measure temperatures as low as 1–1.5 MK from the Yohkoh images.

The present analysis shows that the structures in the solar corona have a wide range of temperatures and that the solar corona is far from uniform in temperature, even within a single loop structure. Since the solar corona consists of magnetic loops, and since these magnetic loops are isolated from each other, the physical conditions (e.g., temperature) of each loop would reflect the present and past local heating rate within the loops. Therefore, it is extremely important that the next-generation solar soft X-ray telescopes should have the capability of observing the entire temperature range of the solar corona in order to solve the coronal heating problem.

## References

Acton L., Tsuneta S., Ogawara Y. et al. 1992, Science 258, 618

Golub L., Herant M. 1989 Proc. SPIE 1160, 629

Hara H., Tsuneta S., Acton L., Bruner M., Lemen J., Ogawara Y. 1994, PASJ 46, 493

Hara H., Tsuneta S., Lemen J., Acton L., McTiernan J. 1992, PASJ 44, L135

Kano R., Tsuneta S. 1994, ApJ submitted

McTiernan J., Kane S., Loran J., Lemen J., Acton L., Hara H., Tsuneta S., Kosugi T. 1993, ApJL 416, L91

Mewe R., Gronenschild E.H.B.M., van den Oord G.H.J. 1985, A&AS 62, 197

Mewe R., Lemen J., van den Oord G.H.J. 1986, A&AS 63, 511

Ogawara Y., Takano T., Kato T., Kosugi T., Tsuneta S., Watanabe T., Kondo I., Uchida Y. 1991 Sol. Phys. 136, 1

Shimizu T. 1995, PASJ 47, 251

Shimizu T., Tsuneta S., Acton L., Lemen J., Ogawara Y., Uchida Y. 1994, ApJ 422, 906

Tsuneta S., Acton L., Bruner M., Lemen J., Brown W., Caravalho R., Catura R., Freeland S. et al. 1991, Sol. Phys. 136, 37

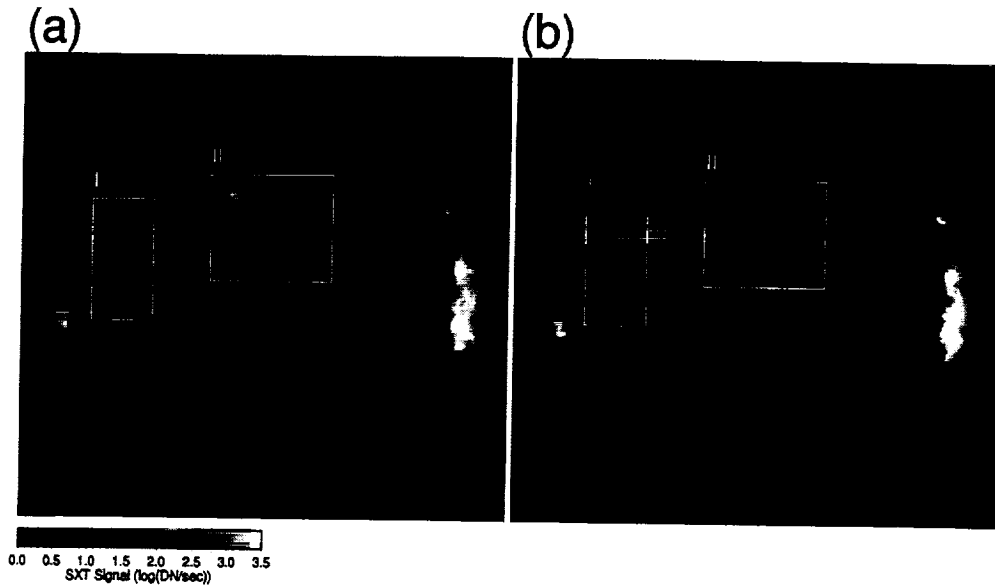Tsuneta S., Hara H., Shimizu T., Acton L., Strong K., Hudson H., Ogawara Y. 1992, PASJ 44, L63

Plate 3



Fig. 2. Whole-Sun images simultaneously taken by Yohkoh and NIXT: (a)Yohkoh SXT, (b) NIXT. North is up and east is to the right. The Yohkoh image was taken at 17:13:19 UT on 1993 April 12; the exposure time is 5.3 s, and the analysis filter is Al/Mg/Mn composite. The NIXT image was taken between 17:17 and 17:23 UT. Figures 3 and 4 show enlarged images of the regions indicated as I and II, respectively.
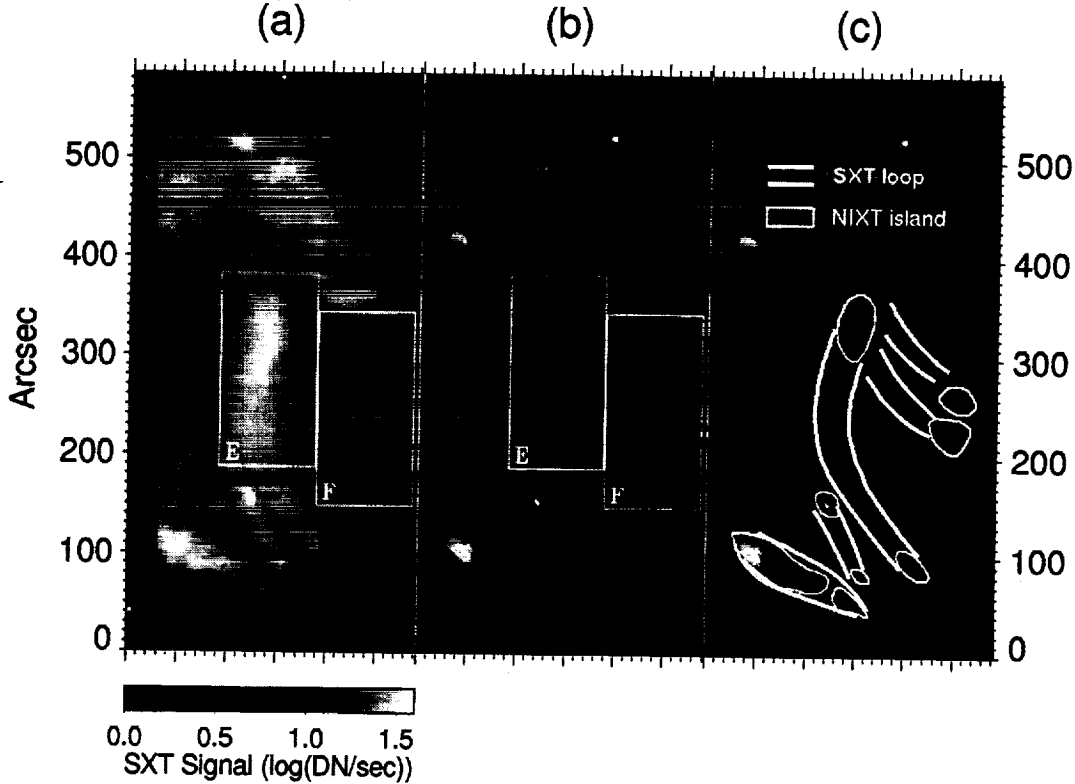


Fig. 3. X-ray images of the quiet region, indicated as I in figure 2: (a) NIXT image, (b) Yohkoh image. (c) The locations of the significant Yohkoh loops are shown by thick lines and the NIXT footpoints by thin lines on the NIXT image. The NIXT image was taken between 17:17 and 17:23 UT. The color changes from black through red, blue, and white with increasing intensity. The Yohkoh image was taken at 17:15:37 UT, and the exposure time is 30.2 s. The analysis filter is Al/Mg/Mn composite. The temperature distributions for the areas indicated by the boxes E and F are shown in figure 5.
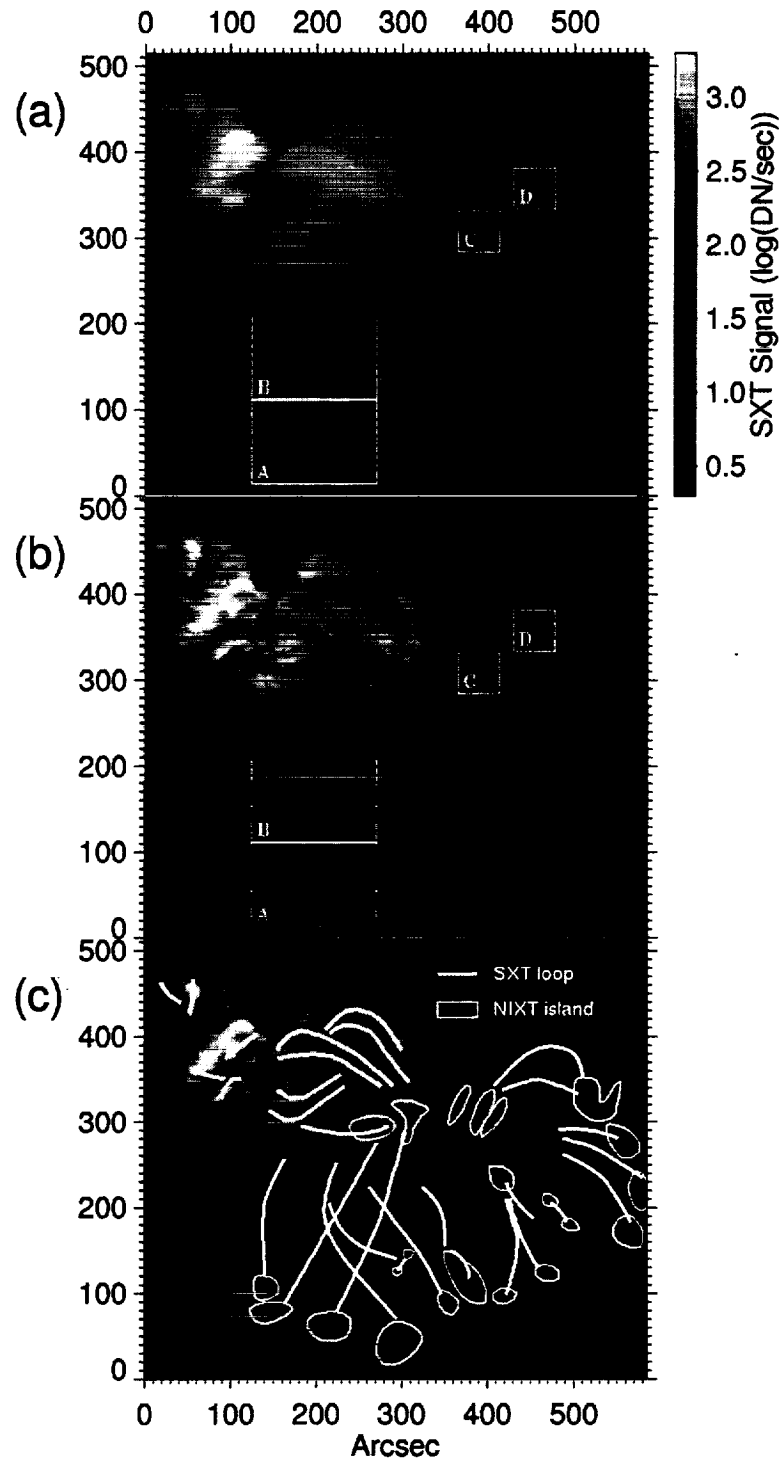
Plate 4



Fig. 4. X-ray images of the region, indicated as II in figure 2: (a) NIXT image, (b) Yohkoh image. (c) The locations of the significant Yohkoh loops are shown by the thick lines and the NIXT footpoints by the thin lines on the NIXT image. The SXT image [panel (a)] was a composite image of three images with different exposures [30.2 s (17:15:37 UT), 5.3 s (17:13:19 UT), 0.17 s (17:11:21 UT) to have a wider dynamic range.] The Yohkoh images with different exposures are combined in panel (a) for the same reason. The analysis filter used is Al/Mg/Mn composite for both images. The temperature distributions for the areas indicated by boxes A, B, C, and D are shown in figure 5.

T. YOSHIDA et al. (see Vol. 47, L17, L18)

# Errata

In the paper "Temperature Structure of the Solar Corona: Comparison of the NIXT and Yohkoh X-ray Images" by T. Yoshida et al. [PASJ **47**, L15–L19 and Plates 3–4 (1995)], the captions of figures 3 and 4 (Plates 3 and 4) should be read as follows:

Fig. 3. X-ray images of the quiet region, indicated as I in figure 2: (a) Yohkoh image, (b) NIXT image. (c) The locations of the significant Yohkoh loops are shown by thick lines and the NIXT footpoints by thin lines on the NIXT image. The NIXT image was taken between 17:17 and 17:23 UT. The color changes from black through red, blue, and white with increasing intensity. The Yohkoh image was taken at 17:15:37 UT, and the exposure time is 30.2 s. The analysis filter is Al/Mg/Mn composite. The temperature distributions for the areas indicated by the boxes E and F are shown in figure 5.

Fig. 4. X-ray images of the region, indicated as II in figure 2: (a) Yohkoh image, (b) NIXT image. (c) The locations of the significant Yohkoh loops are shown by the thick lines and the NIXT footpoints by the thin lines on the NIXT image. The SXT image [panel (a)] was a composite image of three images with different exposures [30.2 s (17:15:37 UT), 5.3 s (17:13:19 UT), 0.17 s (17:11:21 UT) to have a wider dynamic range.] The Yohkoh images with different exposures are combined in panel (a) for the same reason. The analysis filter used is Al/Mg/Mn composite for both images. The temperature distributions for the areas indicated by boxes A, B, C, and D are shown in figure 5.

# DIFFICULTIES IN OBSERVING CORONAL STRUCTURE

L. GOLUB

*Smithsonian Astrophysical Observatory, Cambridge, MA 02128, U.S.A.*

**Abstract.** There has developed in recent years a substantial body of evidence to indicate that the temperature and density structure of the corona are far more complicated than had previously been thought. We review some of the evidence and discuss some specific examples: observations of a limb flare, showing that the cool Hα material is *cospatial* with the hot X-ray emitting material; simultaneous NIXT and *Yohkoh* SXT observations of an active region, showing that loops seen in one instrument are not seen in the other, and that the effect works in *both* directions; comparisons of extrapolated magnetic field measurements to the observed coronal structure, indicating that neither potential nor constant-α force-free fits are adequate. We conclude with a description of two new instruments, the TRACE and the TXI, which will help to resolve some of these difficulties.

## 1. Overview

The importance of magnetic fields in determining the structure of the solar outer atmosphere has long been recognized. Billings (1966) notes that magnetic fields 'are employed, as a matter of fact, to explain all departures from a nonspherical [sic] distribution of matter in the corona, including the loop structure of the corona over active regions...' Observations from sounding rockets in the late 1960s and early 1970s provided convincing evidence that loops structures, apparently outlining the magnetic field direction, are fundamental (Vaiana, Krieger, and Timothy, 1973) and the *Skylab* observations in 1973-1974 provided the impetus for constructing atmosphere models in which loop 'mini-atmospheres' are the fundamental constituent of the inner corona (Rosner, Tucker, and Vaiana, 1978; Craig, McClymont, and Underwood, 1978).

This atmosphere is dynamic and constantly varying. Low (1990) notes that the solar atmosphere is never truly quiescent or static, but adds that for the purpose of building models idealized static states may be used as an approximation to the physics underlying the apparent stability of long-lived structures. The extremely dynamic nature of the corona has been shown most effectively by the Soft X-ray Telescope (SXT) aboard the *Yohkoh* satellite: repeated transient loop brightenings in active regions (Shimizu *et al.* 1992), continual rapid expansion outward of structures at the tops of active regions (Uchida *et al.*, 1992), jets of X-ray emission, apparently associated with reconnection events (Shibata *et al.*, 1992), among others.

Thus, it is already clear that the simplest models of the corona – spherical or plane-parallel – are of limited applicability for interpreting the actual observations, and that the simplest loop atmosphere models – static loops – are also of limited usefulness. To these complications, we will add an additional set of worries, by

Table I

Observational questions about the solar corona

| Q1. | Is the corona hot or cold at a given point in space? | A1. | Depends on the viewing method. |
|-----|-----|-----|-----|
| Q2. | Where is the 'base' of the corona? | A2. | Meaningful only for individual loops and probably unanswerable. |
| Q3. | What is the transverse scale size of coronal structures? | A3. | Our knowledge is limited by present instrumental resolutions. |
| Q4. | What is the relation between the coronal B and X-ray emission? | A4. | Data do not provide sufficient constraints. |
| Q5. | What does the hot corona look like? | A5. | Depends on the viewing method. |

showing that it is not at all clear that we are even now in a position to say that we know what coronal loops look like, or to know how the real corona is constructed of such loops.

## 2. Case Studies

In order to illustrate the difficulties alluded to in the Overview, we will examine five specific 'case studies,' each involving a seemingly reasonable question about the corona. The questions addressed by these studies are listed in Table I, along with the answer to each question. The latter will be explained in the course of discussing each case. These examples are all taken from work related to flights of the Normal Incidence X-ray Telescope (NIXT) sounding rocket payload (Golub *et al.*, 1990) during the years 1989–1993.

### 2.1. A LIMB FLARE

On 11 Sept. 1989, the NIXT rocket was launched at the start of a small flare (GOES classification C5). However, during the five-minute flight, a second flare began in an active region at the limb (Herant *et al.*, 1991). Examination of the GOES X-ray light curves (Figure 1) indicates that the limb flare began at about 16:36 UT during the decay phase of the larger on-disk flare. The NIXT observations also began at 16:36 UT, with the last image taken at 16:41:35 UT; the peak of the limb flare in X-rays is at ~16:42 UT. Thus, the NIXT coverage could not have been better-timed.

Figure 2 shows simultaneous H$\alpha$ and X-ray images of the flare at the time of the peak. The most striking aspect of this event seems to be the nearly identical size, shape and location of the flare in the two wavelength regimes. This similarity is confirmed by a cross-correlation between the two datasets, shown in Figure 3. The contour lines show the X-ray brightness and the shaded region shows the H brightness: the two overlap to within the accuracy of alignment. Thus it would
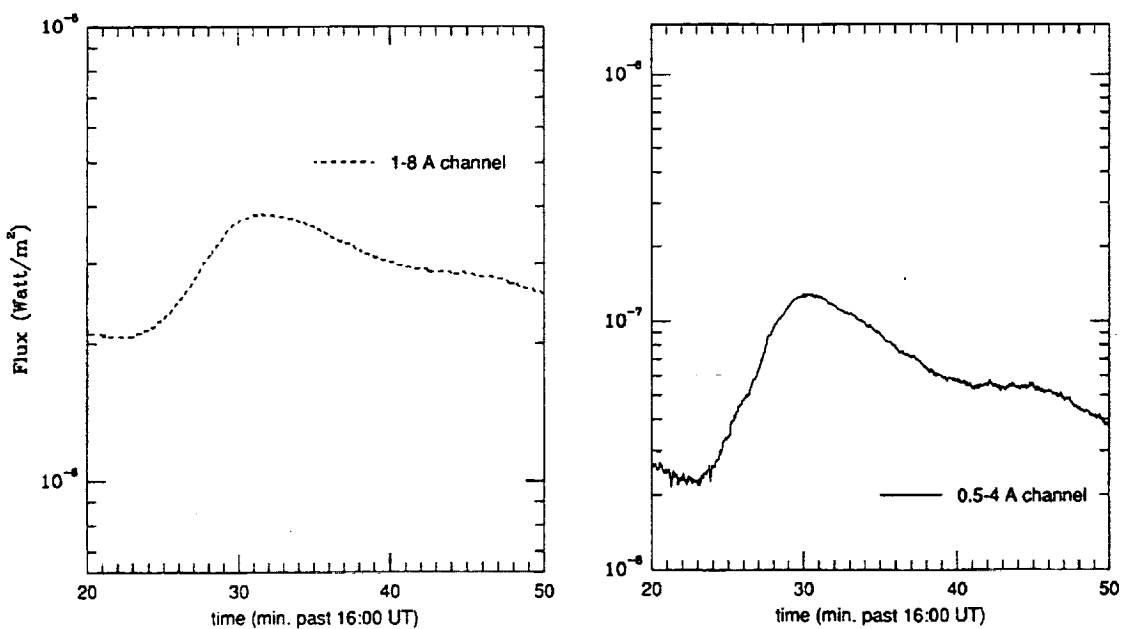
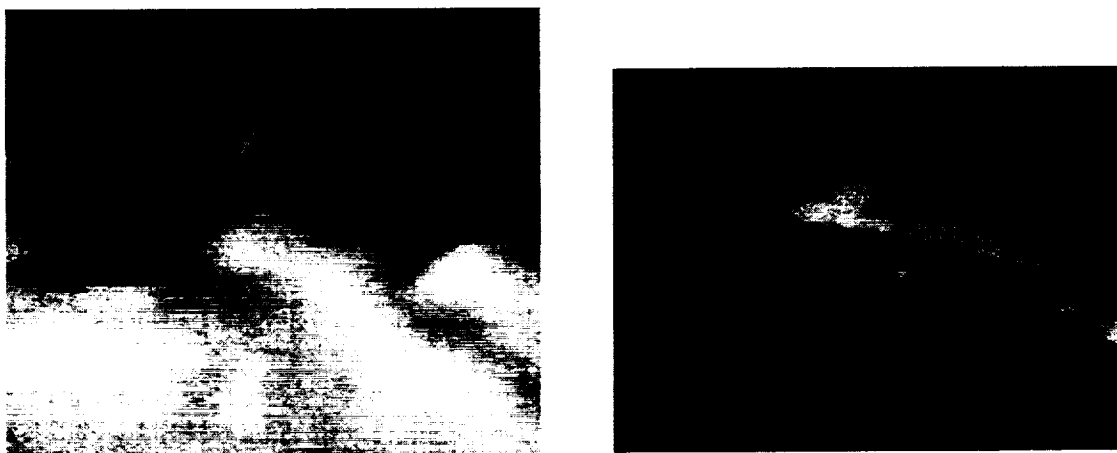*Figure 1.* GOES 1–8 Å and 0.5–4 Å X-ray plots for 9 November, 1989.



*Figure 2.* Simultaneous Hα and NIXT X-ray images of a limb flare.

appear that the corona is both hot (X-ray) and cool (Hα) at the same place at the same time.

Possible explanations exist, of course, for this apparent contradiciton. It is possible that the X-ray emission originates from a thin shell ahead of the advancing Hα region. Alternatively, hot and cool material may be intermingled on small spatial scales within the observed regions. The problem is not to come up with an answer, it is to come up with a correct answer.
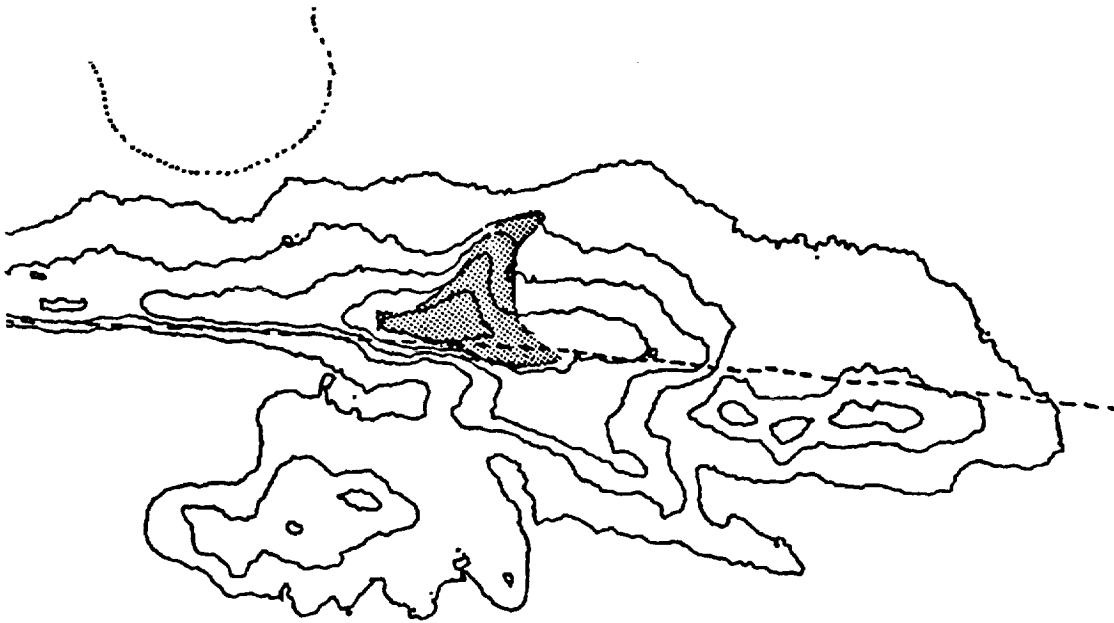
*Figure 3.* Relative positions of X-ray event and Hα material.

## 2.2. SIMULTANEOUS WHITE-LIGHT AND X-RAY IMAGING

Plane-parallel, or spherically symmetric models of the outer solar atmosphere treat the relation between temperature and height as one-dimensional, although not monotonic since the temperature at first increases with height but then decreases again. With the advent of loop model atmospheres, as described above, this fundamental view did not change in essence, but the temperature vs height relation is transplanted into each loop instead of into the atmosphere as a whole. However, a flight of the NIXT payload on 22 February 1991 provided a unique dataset which shows that a more complicated geometry is required in order to explain the observations.

The multilayer mirrors used in the NIXT to provide X-ray imaging also reflect visible light with $\approx$ 50% reflectivity. In order to record only the (much fainter) X-ray image, two stages of visible-light rejection are employed: an entrance aperture filter, which cuts the visible to $\approx$ 1% and a focal plane filter, which provides $10^9$ reduction in the visible. During the launch phase of the February 1991 flight, a portion of the entrance aperture filter broke. The instrument, however, was designed so that the focal plane filter acts as back-up in the event of just such a failure. Thus, because the X-rays and the visible are reflected in the same way from the same mirror at the same time, we obtained simultaneous images of the visible disk and the corona. These are automatically coaligned and have the same plate scale, so that high precision (<1 arc sec) comparison between the two can be made.

Figure 4 shows a portion of the east limb from one of the exposures obtained on that flight. Note that there is a dark band at the limb, between the white-light solar limb and the bright coronal X-ray emission. We note several features of this

*Figure 4.* Portion of a combined NIXT/white-light image, showing a gap between the visible limb and the 'base' of the corona, 22 February, 1991.

gap: (1) it is most clearly evident when there is an X-ray emitting region behind the limb and no emitting region in front of the limb; (2) the thickness of the gap varies between equator and poles, or between active regions and large scale 'quiet' regions; (3) at both the inner (white light) and outer (X-ray) heights, the gap is quite sharp. The question we will address is, how is this gap to be interpreted?

The data from this flight have been analyzed by Daw, DeLuca, and Golub (1995), who find that a model in which the corona is viewed as consisting of a homogeneous set of loops, with temperature varying as a function of height in a uniform manner (Figure 5(a)) is not consistent with the data. In order to explain what is seen, it is necessary to use a model in which hot loops penetrate downward into an atmosphere having cool spicular material penetrating upward (Figure 5(b)). The two types of loops do not connect physically, but are interspersed along the line of sight. Thus, the gap is interpreted as the upward extent of spicular material, viewed along the line of sight at the limb and absorbing the X-rays emanating from loops behind the spicules.

We note that the soft X-rays in the NIXT data are strongly absorbed in spicular material, with about 10 arc sec path length required for $e^{-1}$ absorption. The variation in thickness of the band indicates that spicules may extend farther in open field (e.g., coronal hole) regions than in higher temperature closed-loop regions, as reported by Huber *et al.* (1974). This interpretation of the NIXT data suggests that the footpoints of coronal loops cannot, in principle, be seen. When viewed at the limb,
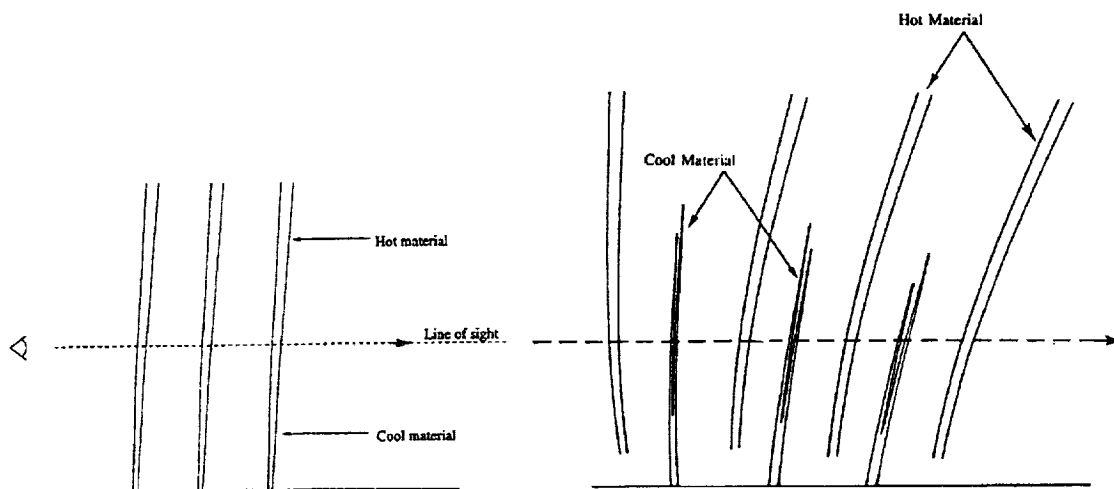
*Figure 5.* Two loop model atmospheres offering alternative explanations of the gap seen in Figure 4. Modified plane-parallel model on left does not fit the data.

they are obscured by the intervening spicule material; when viewed from above, the projection angle is such that the height of the coronal 'base' is very poorly determined. Depending upon the relative spatial density of hot vs cool structures, there may be a small range of locations near the center of the disk which allow for both viewing the loops at an angle and for viewing them unobstructed. However, this is not yet known.

### 2.3. ACTIVE REGION FINE STRUCTURE

The progress in X-ray optics, when applied to solar coronal imaging, has consistently revealed coronal fine structure down to the resolution limit of the observing instruments (see, e.g., articles by Giacconi, Golub, and Walker *et al.* in Linsky and Serio, 1993). An example is shown in Figure 6, a coronal X-ray image from the NIXT instrument, obtained on 11 July, 1991. There is clearly fine structure prevalent everywhere in the image and photographic analysis indicates that it reaches the combined limit set by the film and by the pointing stability of the rocket.

A quantitative analysis of the fine structure of several active regions observed by the NIXT was carried out by Gómez, Martens, and Golub (1993). By Fourier analyzing the images, they find a broad, isotropic power-law spectrum for the spatial distribution of soft X-ray intensities. The spectrum has a slope of $\alpha \approx -3$, which extends down to the resolution limit of the instrument at $\approx 0.75$ arc sec.

A similar result has been obtained by Martens and Gómez (1992) from analysis of *Yohkoh* SXT data: the Fourier transform distribution is a power law (with somewhat smaller slope of $\approx -2.4$) which extends down to the Nyquist frequency. Thus, for both cases in which the procedure has been carried out, the spatial structuring of the corona is seen to be limited by the resolution of the imaging instrument. The implication, since the Sun does not know what instrument we are
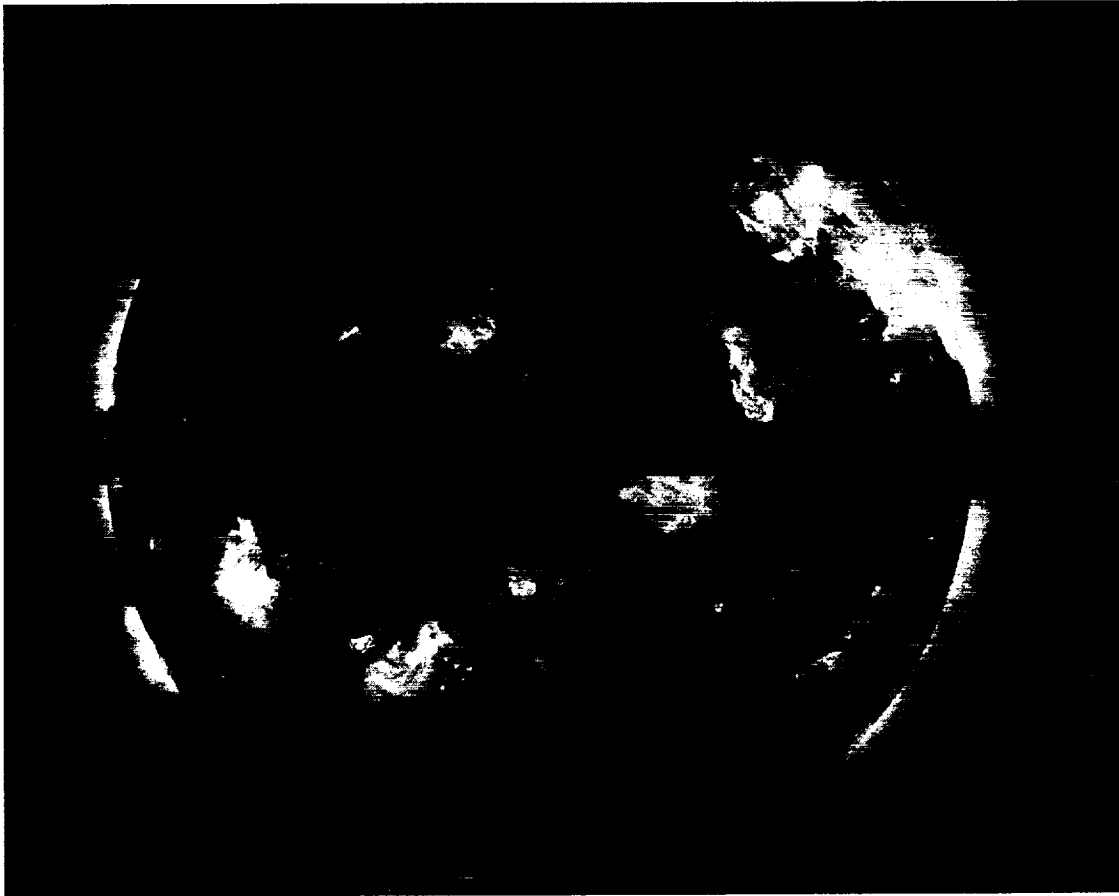
*Figure 6.* 11 July, 1991 NIXT image.

using to observe it, is that we have not yet fully resolved the coronal fine structure. Thus, the answer to Question 3, 'What is the transverse scale size of coronal structures?', is that we do not yet know.

## 2.4. MAGNETIC FIELD EXTRAPOLATION VS OBSERVED STRUCTURE

There have been only a limited number of attempts in recent years to carry out direct comparisons between high resolution coronal observations and magnetic field extrapolations, if we exclude attempts to explain the onset of flares by testing the non-potentiality of fields. For non-flaring regions, i.e., normal coronal structure, Poletto *et al.* (1975) and Sakurai and Uchida (1977) had reasonable success at the level of late 1960s and early 1970s resolution. More recently Sams, Golub, and Weiss (1993) found a general agreement between extrapolations and the structures seen in the NIXT, although close examination shows that the agreement is quite poor in detail. Metcalf *et al.* (1994) conclude, from comparison of vector magnetograph data (giving the locations of vertical currents) with *Yohkoh* SXT coronal data, that there is a very poor spatial and temporal correlation between the locations of the currents and the locations of bright coronal structures.
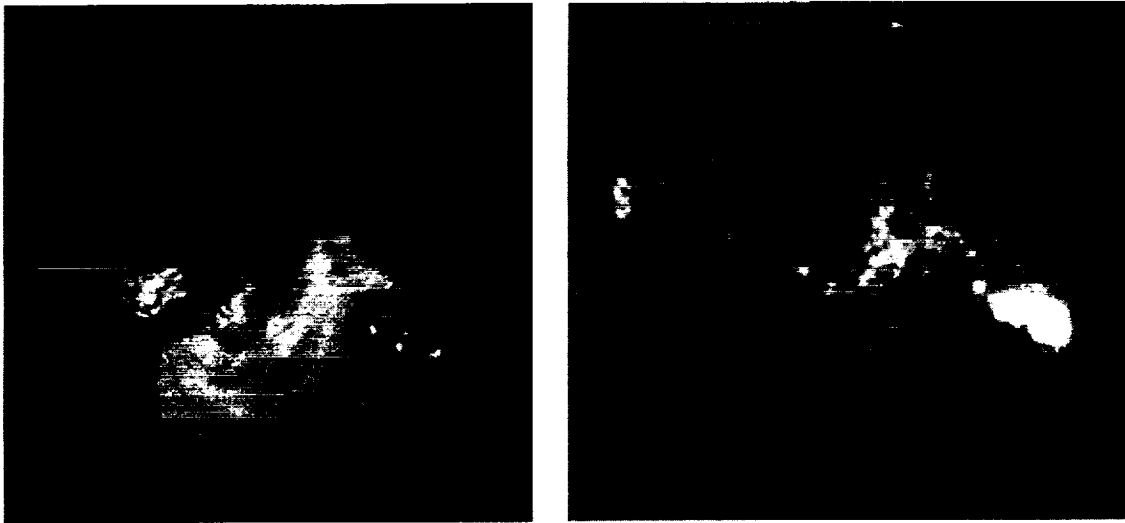
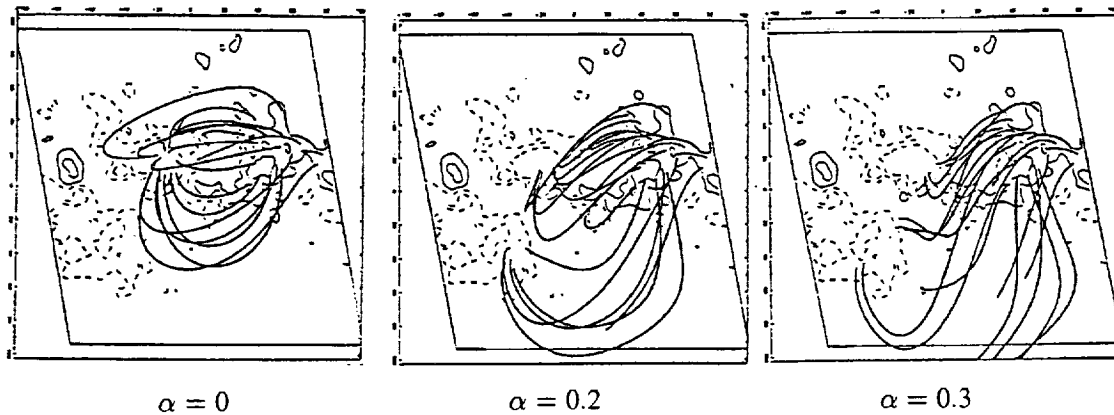Figure 7. NIXT X-ray image of AR 6718 and KPNO magnetogram of the region.



$\alpha = 0$                    $\alpha = 0.2$                    $\alpha = 0.3$

Figure 8. Magnetic field extrapolations of AR 6718, with three values of $\alpha$.

In a recent study, Schmieder *et al.* (1996) have used high resolution NIXT data combined with Kitt Peak magnetogram and Multi-channel Double Pass (MSDP) spectrograph data, to study in more detail the relationship between the observed structure and the type of magnetic field extrapolation employed. The extrapolation code is based on the work of Alissandrakis (1981) as modified by Démoulin *et al.* (1996). A single active region, AR 6718 on 11 July, 1991, was chosen for study; an X-ray image of the region and the corresponding portion of the magnetogram are shown in Figure 7.

The first result is that a potential-field extrapolation does not represent the observed coronal structure at all, and that even a constant-$\alpha$ force-free field extrapolation is not adequate. Figure 8 shows extrapolations using three values of $\alpha$. The left-most panel shows $\alpha = 0$, i.e., a potential field. Note that the connectivity of the field lines is entirely different from that of the observed structures. The two force-free fits in the middle and right-hand panels match portions of the region,
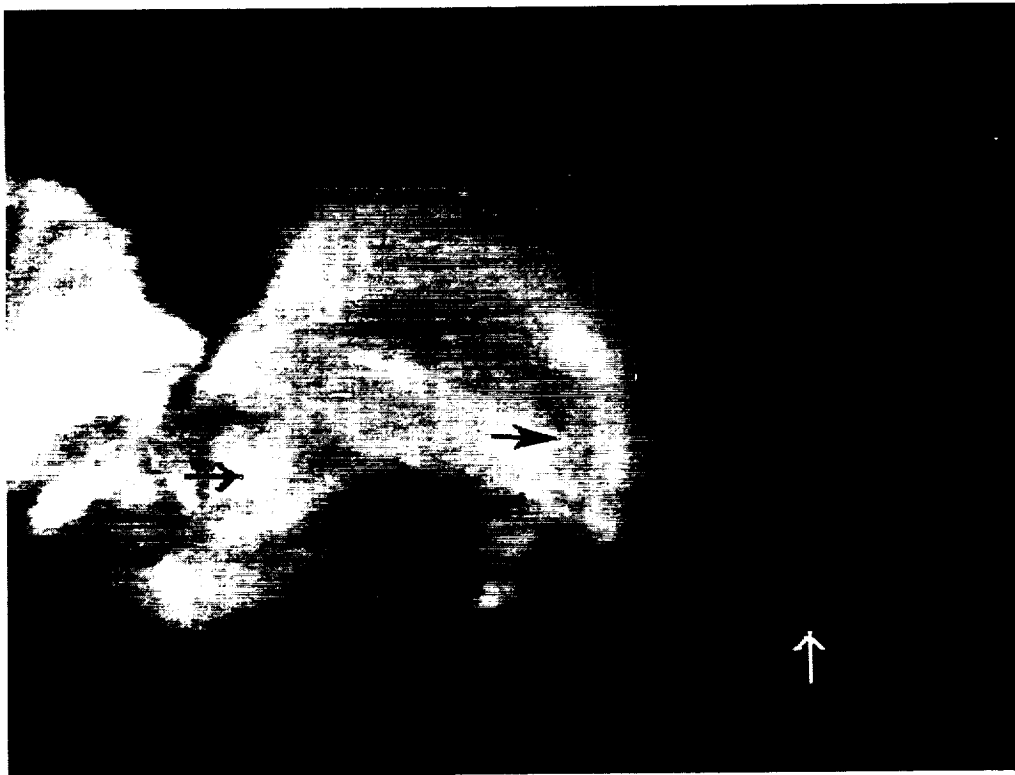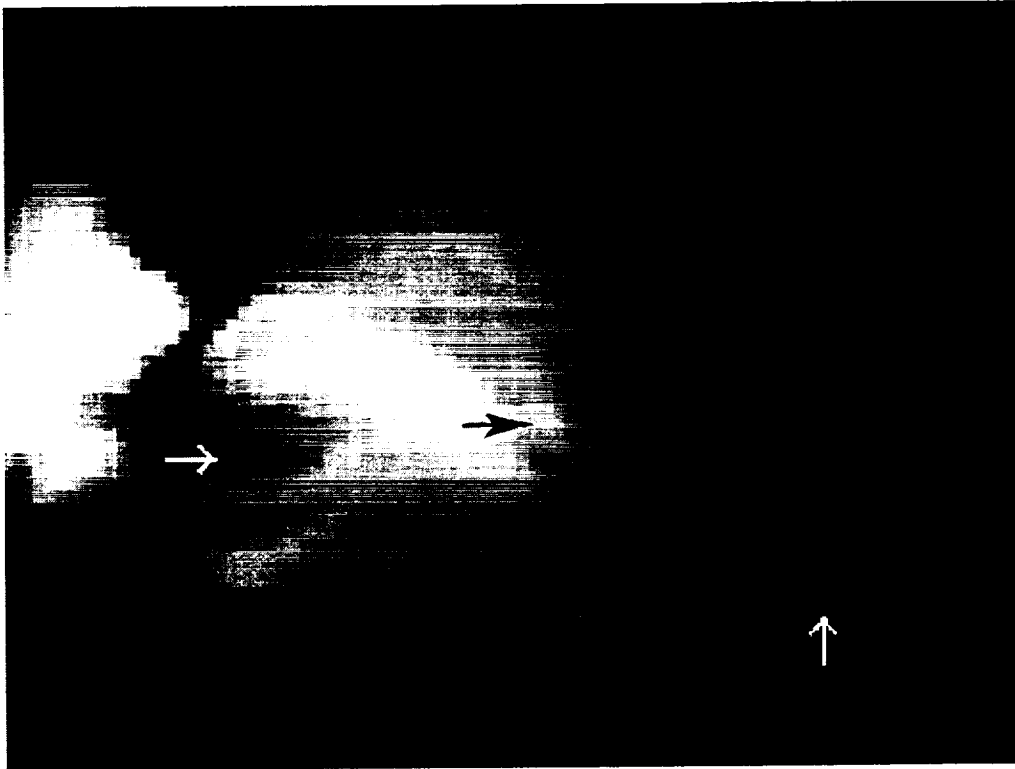
*Figure 9.* Comparison between *Yohkoh* (*top*) and NIXT (*bottom*) observations of an active region; arrows indicate structures seen in one of the instruments but *not* seen in the other.

but neither one in itself is a good fit. What we find is that the inner portion of the active region is well matched by the larger value of $\alpha$ while the outer portion of the region is matched by a lower $\alpha$.

A possible interpretation of this result is that there is, with time, a relaxation of the magnetic field, as proposed by Heyvaerts and Priest (1984). In a highly-conducting plasma, small-scale processes dissipate magnetic energy much more rapidly than helicity $H \equiv \int \mathbf{A} \cdot \mathbf{B} \, dV$ (Taylor, 1974; Berger, 1985). With this constraint the magnetic field does not relax to a potential state, but to a linear force-free state. The gradient of $\alpha$ found in this region may be indicative of this ongoing relaxation process.

### 2.5. *Yohkoh* SXT vs NIXT COMPARISON

In April 1993 the *Yohkoh* SXT carried out a special observing sequence simultaneous with a flight of the NIXT rocket. An inital comparison of the two datasets was carried out by Yoshida *et al.* (1995) for a quiet corona region. Because the SXT temperature response is somewhat harder than that of the NIXT ($>2.5$ MK for SXT vs 1–3 MK for NIXT) it was expected that the SXT would see the hotter top portions of coronal loops while the NIXT would see the lower portions or the footpoints. This was indeed generally seen to be the case in that study.

However, subsequent evaluation of the one active region on the disk on that day is showing a completely different and unexpected result. One expects that 'all X-ray images are alike,' so that the two should show roughly similar structures. Viewed from a distance, the two observations seem to be showing the same coronal features. However, detailed examination shows some remarkable discrepancies between the two.

Figure 9 shows the comparison of NIXT and *Yohkoh* SXT observations, with arrows pointing to three locations in the region. These are places where a structure or set of structures is visible in one of the images and *entirely invisible* in the other; the effect works both ways. Thus, if only one of these images were available, we would draw reonneous conclusions about the coronal structure, since there would be no indication at all that some structures are present.

The seriousness of this problem is obvious: if we intend to study the formation, stability and dynamics of coronal structures, one must first be able to see them. A partial solution to this problem is described in the next section.

## 3. Some Partial Solutions

The above discussion provides only a partial listing of some of the problems we are encountering in attempting to study the formation, heating, structuring and dynamics of the solar corona. In this section we describe two new instruments which will help to solve, or at least advance, some of these problem areas. The

TRACE instrument will have the highest spatial resolution ever used to observe the corona, as well as the ability to discriminate multiple temperature regimes and to view the atmosphere from the upper chromosphere up into the active region corona. The TXI is a rocket-borne payload which will have the capability of observing the entire sequence of successive ionization stages of a single element from $<10^6$ K to $>3 \times 10^6$ K, and will also determine flow velocities at these temperatures.

## 3.1. TRACE

The Transition Region And Coronal Explorer (TRACE) is designed to explore quantitatively the connections between fine-scale magnetic fields at the solar surface and the associated plasma structures in the solar outer atmosphere. The TRACE instrument uses multiple UV and normal-incidence XUV channels to collect images of atmospheric plasma from $10^4$ K to $10^7$ K. Many of the physical problems that arise in this portion of the atmosphere – plasma confinement, reconnection, wave propagation, plasma heating – arise throughout space physics and much of astrophysics as well. Although recent progress in, e.g., numerical MHD simulations has been substantial (viz., Low, 1990), use of these models requires close guidance by the observations, because the enormous range in parameter scale sizes cannot be realized in the computations.

The telescope provides true 1 arc sec resolution (1 pixel is 0.5 arc sec) and temporal resolution as short as a fraction of a second for bright sources. Table II lists the operating spectral bands, the associated temperatures and the portions of the atmosphere covered. The instrument uses four normal incidence coatings, one for broadband UV and three for narrow band XUV operation. The UV channel includes a set of narrow-band filters at the focal plane, thereby allowing sub-channels which detect portions of the atmosphere from the photosphere to the transition region. Selection of the XUV channels is based on a thorough analysis carried out by Golub, Hartquist, and Quillen (1989), who analyzed the spectral region accessible to normal incidence techniques and determined the best lines to use for particular atmospheric features of interest.

TRACE is launched on a Pegasus-XL into a polar, Sun-synchronous orbit, thereby providing continuous observation of the Sun. Continuous observing for about 8 months is planned over a 1-year baseline mission. TRACE produces data complementary with SOHO, and planning of the TRACE daily observations is being coordinated with those of SOHO.

The main components of the TRACE instrument are shown in Figure 10. The TRACE instrument consists of a 30-cm diameter Cassegrain telescope and a filter system feeding a CCD detector. Each quadrant of the telescope is coated for sensitivity to a different wavelength range. Light entering the instrument passes first through an entrance filter assembly which transmits only UV and soft X-ray radiation, thus blocking the solar heat from reaching the mirrors. A large rotating

Table II

TRACE spectral regions and observing parameters

| Central wavelength (Å) | Width (Å) | Ion | Location |
| --- | --- | --- | --- |
| 2500 | Broad | Continuum | Photosphere |
| 1700 | Broad | $T_{min}$/Chrom. | |
| 1570 | 30 | C I, Fe II, Cont. | Photosphere |
| 1550 | 30 | C IV | Transition region |
| 1216 | 84 | H Lα | Chromosphere |
| 284 | 14 | Fe XV | Corona |
| 195 | 10 | Fe XII | Corona |
| | | (+Fe XXIV) | Flares |
| 171 | 9 | Fe IX | Corona |
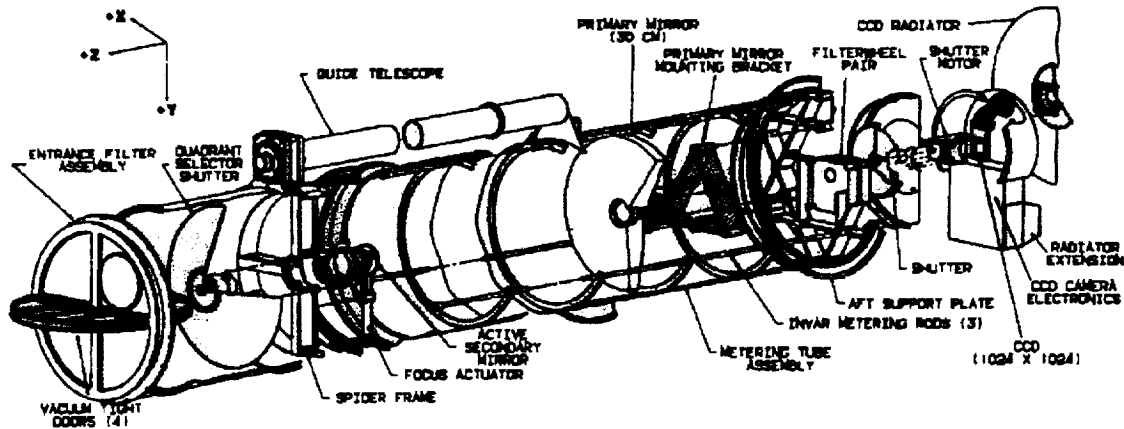


Figure 10. Major system components of the TRACE instrument.

quadrant shutter selects one quadrant at a time for viewing. The secondary mirror of the telescope is active, to correct for pointing jitter to better than 0.1 arc sec.

The converging beam from the secondary mirror passes through the central hole in the primary, where it encounters two filter wheels in series, each having three filters and one open position. These wheels contain both the XUV light-blocking and the UV passband filters. Finally, there is a focal plane shutter and a 1024 × 1024 CCD, for a field of view of 8.5 × 8.5 arc min. Mosaic observations are planned, for larger field and daily full disk data-taking. The TRACE launch is late in 1997, and mission lifetime is at least 8 months. Thus it will be observing during the rise phase of the new solar cycle.

Some of the scientific objectives of the mission are:

- Magnetic field structure and evolution.
- Coronal heating and magnetic fields.
- Onset of coronal mass ejections.
- Variability of X-ray bright points.

The mission and its objectives are described in more detail in Tarbell *et al.* (1994).

## 3.2. TXI

The Tuneable X-ray Imager (TXI) is a high-resolution coronal imaging instrument which has the ability to produce near-monochromatic images tuneable over a range of XUV wavelengths. The present design covers the wavelength range 170–220 Å, which includes the strong series of iron lines from Fe IX through Fe XIV, inclusive. Thus, the problem of 'missing' structures is solved, for the temperature range $\log T = 5.8$–$6.4$, because all of the successive ionization stages are isolated and recorded.

Figure 11 shows a schematic layout of the instrument. Spectral isolation is achieved by using a double-crystal monochromator, which feeds a broadband telescope, coated with an XUV multilayer having $\Delta\lambda \sim 30$ Å (FWHM). The monochromator is made as narrow-band as possible, which in this instance is $\approx 4$ Å, and it is tuned by rotating the two plane mirrors in parallel. A Cowan–Golovehenko arrangement is used (Cowan, 1983), which has the highly desireable property that the entrance and exits beams stay fixed during tuning. Thus, there is no image motion in the focal plane as the wavelength is changed.

Table III shows the strongest lines in the TXI passband. Depending upon line strength and available exposure time, it appears possible to record data out to $\approx 220$ Å; no data below 170 Å are recorded because aluminum light-blocking filters are used at the entrance aperture and at the focal plane. We note that line multiplets, such as Fe XII near 193 Å, do not smear the image, because this is a non-dispersive system.

The TXI sounding rocket program has just received approval from NASA to begin construction (May 1996). Present plans are to have the payload ready to fly by the summer of 1998. A summer launch is neccessary in order to reduce absorption by the residual atmosphere even at rocket altitudes. A minimum altitude of 100 miles is necessary for the wavelengths observed in this experiment, and a line of sight to the Sun as near normal to the plane of the atmosphere as possible is required. The launch therefore takes place around local noon in White Sands, NM.

### 3.3. THE SOLAR RADIO TELESCOPE

Of course, it is not only in the area of space-based instrumentation that solutions to the present set of problems in solar physics may be sought. In this section we describe a representative ground-based instrument, designed to map the magnetic field structure and topology in the corona.

A proposal for a dedicated Solar Radio Telescope which represents a major advance on current radio facilities is currently being explored (a report by D. Gary and T. Bastian will be available shortly). The ability to map solar magnetic fields
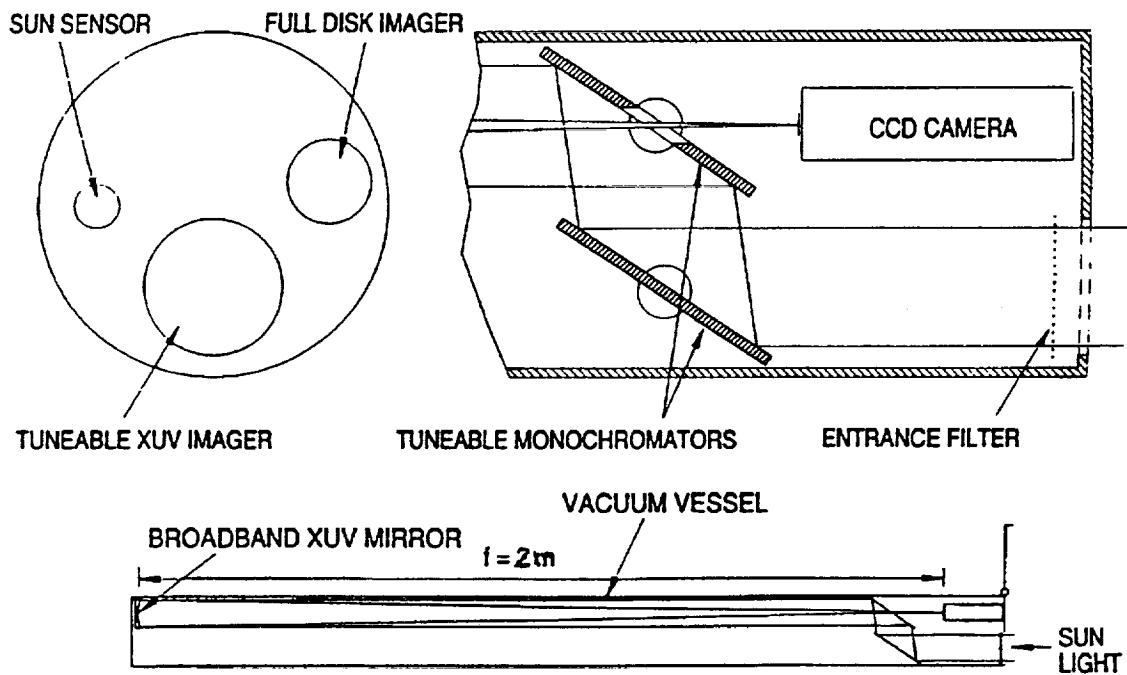
*Figure 11.* Schematic layout of the Tuneable XUV Imager.

Table III
Strongest lines in the TXI passband

| Ion | Wavelength (Å) | $\log T$ |
|-----|----------------|----------|
| Fe IX | 171.08 | 6.0 |
| O V | 172.17 | 5.4 |
| O VI | 172.94 | 5.5 |
|  | 173.08 |  |
| Fe X | 174.53 | 6.1 |
|  | 177.24 |  |
| Fe XI | 180.42 | 6.2 |
| Si XI/Fe XII | 186.88 | 6.2 |
| Fe XI | 188.22 | 6.2 |
| Fe XXIV | 192.03 | 7.3 |
| Fe XII | 192.40 | 6.2 |
|  | 193.52 |  |
|  | 195.13 |  |
| Fe XIII | 202.04 | 6.2 |
|  | 203.82 |  |
| Fe XIV | 211.32 | 6.3 |
| He II | 237.35 | 4.7 |

above coronal active regions is one of the major goals of this telescope. The features necessary to carry out such a goal are:

– the ability to make radio images of active regions on short time scales with high spatial resolution and high dynamic range;

– the ability to make images at many closely-spaced frequencies across a broad frequency range nearly simultaneously; and

– accurate polarimetry.

The proposed instrument which provides these features consists of an array which contains many small dishes (presently planned to be 40) with full-disk coverage, three large ($\sim$25 m) dishes to provide sensitivity and allow accurate calibration, and receivers which incorporate the frequency agile characteristics so successfully demonstrated by the OVRO array with a target range from 300 MHz to 30 GHz. This instrument would have 2.5 times as many baselines as the VLA, and requires a large correlator to handle them. Recent advances in broadband microwave components, large correlators and computers make such an instrument possible for a low cost. Considerable effort will also be expended on software for real-time processing of the data into a form (images and coronal field maps) suitable for immediate use by the broader solar community.

### 3.3.1. *Vector Magnetic Fields*

Finally, we mention the almost obvious point that vector magnetograms are crucially important in the comparison between surface fields and coronal structure/stability. Ground-based observations have progressed enormously, but there still remains the basic question: how much of the observed variability is due to atmospheric effects and how much is intrinsic to the source? This question has been answered in part by comparing observations taken simultaneously at widely-separated sites. However, the best way to answer the question and to obtain the highest quality observations, is to place a vector magnetograph in orbit.

### Acknowledgements

### References

Alissandrakis, C. E.: 1981, *Astron. Astrophys.* **100**, 197.
Berger, M. A.: 1985, *Astrophys. J. Suppl.* **59**, 433.
Billings, D. E.: 1966, *A Guide to the Solar Corona*, Academic Press, New York.
Craig, I. J. D., McClymont, A. N., and Underwood, J. H.: 1978, *Astron. Astrophys.* **70**, 1.
Daw, A., DeLuca, E., and Golub, L.: 1995, *Astrophys. J.* **453**, 929.
Démoulin, P., Balala, L. G., Mandrini, C. H., Hénoux, J. C., and Rovira, M. G.: 1996, *Astron. Astrophys.*, in press.
Golub, L., Hartquist, T. W., and Quillen, A. C.: 1989, *Solar Phys.* **122**, 245.
Golub, L., Herant, M., Kalata, K., Lovas, S., Nystrom, G., Pardo, F., Spiller, E., and Wilczynski, J.: 1990, *Nature* **6269**, 842.

Gómez, D. O., Martens, P. C. H., and Golub, L.: 1993, *Astrophys. J.* **405**, 767.

Herant, M., Pardo, F., Spiller, E., and Golub, L.: 1991, *Astrophys. J.* **376**, 707.

Heyvaerts, J. and Priest, E. R.: 1984, *Astrophys. J.* **137**, 63.

Huber, M. C. E., Foukal, P. V., Noyes, R. W., Reeves, E. M., Schmahl, E. J., Timothy, J. G., Vernazza, J. E., and Withbroe, G. L.: 1974, *Astrophys. J.* **194**, L115.

Linsky, J. F. and Serio, S. (eds.): 1993, *Physics of Solar and Stellar Coronae*, Kluwer Academic Publishers, Dordrecht, Holland.

Low, B. C.: 1990, *Ann. Rev. Astron. Astrophys.* **28**, 491.

Martens, P. C. H. and Gómez, D. O.: 1992, *Publ. Astron. Soc. Japan* **44**, L187.

Metcalf, T. R., Canfield, R. C., Hudson, H. S., Mickey, D. L., Wülser, J. P., Martens, P. C., and Tsuneta, S.: 1994, *Astrophys. J.* **428**, 860.

Poletto, G., Vaiana, G. S., Zombeck, M. V., Krieger, A. S., and Timothy, A. F.: 1975, *Solar Phys.* **44**, 83.

Rosner, R., Tucker, W. H., and Vaiana, G. S.: 1978, *Astrophys. J.* **220**, 643.

Sakurai, T. and Uchida, Y.: 1977, *Solar Phys.* **52**, 397.

Sams, B. J., III, Golub, L., and Weiss, N. O.: 1993, *Astrophys. J.* **399**, 313.

Schmieder, B., Démoulin, P., Aulanier, G., and Golub, L.: 1996, *Astrophys. J.*, in press.

Shibata, K. *et al.*: 1992, *Publ. Astron. Soc. Japan* **44**, L173.

Shimizu, T., Tsuneta, S., Acton, L. W., Lemen, J. R., and Uchida, Y.: 1992, *Publ. Astron. Soc. Japan* **44**, L147.

Tarbell, T. D., Bruner, M., Jurcevich, B., Lemen, J., Strong, K., Title, A., Wolfson, J., Golub, L., and Fisher, R.: 1994, *Proc. of the 3rd SOHO Workshop*, ESA SP-373.

Taylor, J. B.: 1974, *Phys. Rev. Letters* **33**, 1139.

Uchida, Y., McAllister, A., Strong, K. T., Ogawara, Y., Shimizu, T., Matsumoto, R., and Hudson, H. S.: 1992, *Publ. Astron. Soc. Japan* **44**, L155.

Vaiana, G. S., Krieger, A. S., and Timothy, A. F.: 1973, *Solar Phys.* **32**, 81.

Yoshida, T., Tsuneta, S., Golub, L., Strong, K., and Ogawara, Y.: 1995, *Publ. Astron. Soc. Japan* **47**, L15.

# NIXT X-Ray Bright Point Survey:
# Observation and Classification of Data from 12 April 1993

M. J. Wills

Montana State University, Physics Department, EPS 259, Bozeman, MT 59717

M. D. Hartl

University of Maryland, Physics Building, College Park, MD 20742

E. E. DeLuca, L. Golub

Harvard-Smithsonian Center for Astrophysics, 60 Garden Street, Cambridge, MA 02138

and A. Daw

Department of Physics, Harvard University, Cambridge, MA 02138

## 1. Introduction

X-ray bright points (XBPs) are compact, isolated x-ray structures seen in images of the x-ray coronaGolub, et al. 1974). Over the past twenty years, they have been observed by various instruments sensitive to 2 million degree plasma, such as SoHO/EIT, *Yohkoh*, NIXT, MSSTA, HRTS, and Skylab, resulting in an abundance of data. XBPs are thought to have characteristic sizes of 10–30", although this range is not strictly adhered to (Parnell, Priest, & Golub 1994). Detailed studies of individual bright points reveal that they are prone to variability and can possess intricate loop structures (Parnell, Priest, & Golub 1994; Strong, et al. 1992; Sheeley & Golub, 1979).

One line of research on XBPs examines them as part of global solar phenomena. Early XBP studies suggested that their abundance is anti-correlated with the number of observed active regions and therefore XBPs follow an inverse solar cycle (Golub, et al. 1990; Golub 1980; Golub, Davis, & Krieger 1979). Recent work by Harvey & Strong (personal communication) using *Yohkoh* data reveals a leveling-off of bright point numbers which may signal a deviation from this cyclical trend, or possibly a lack of correlation entirely. The resolution of an apparent conflict between the Skylab and *Yohkoh* results remains elusive.

Other studies have focused on the mechanisms powering XBPs. Most models focus on the solar magnetic field as the source of XBP brightening. Studies using magnetograms have found that XBPs are generally associated with bipolar magnetic structures (Moses, et al. 1994; Webb, et al. 1993; Webb & Moses 1989; Webb & Moses 1990; Golub, Harvey, & Webb 1986; Tang, et al. 1982; Golub 1980; Golub, Davis, & Krieger 1979); moreover, comparisons between soft x-ray data and time-resolved magnetograms show that the magnetic dynamics most often associated with bright points are converging flux regions (Moses, et al. 1994; Webb, et al. 1993; Webb & Moses 1989; Webb & Moses 1990). This has led to the development of a converging flux model (Priest, Parnell, & Martin 1994), which hypothesizes magnetic reconnection of opposite polarity magnetic fields as the source of bright point heating. This model continues to be developed, with the most recent work focusing on modeling three-dimensional bright point structure (Parnell, Priest, & Golub 1994) and unequal bipolar cancellation sources (Parnell, Priest, & Titov 1994).

The aim of our study is to examine the morphology of XBPs together with the nature of the underlying magnetic structure. In addition, due to the large number of XBPs visible in the 12 April 1993 NIXT photographs, we are able to determine estimates for parameters relevant to theoretical bright point models: the fraction of bright points with clear bipolar signatures, characteristic angular size, and emitted energy flux. The large number of bright points in our study allows us to determine statistically significant XBP

distributions by solar latitude.

## 2. Observational Procedures

Our study focuses on full-disk soft x-ray images taken by the Normal Incidence X-ray Telescope (NIXT) payload during a sounding rocket flight launched on 12 April 1993 at **1715 UT** from the White Sands Missile Range in New Mexico. The NIXT instrument operates at 63.5 Å in order to image the Fe XVI and Mg X spectral lines (. This allows for an observing range of 1–3 million degrees (Golub & Pasachoff, 1997). NIXT observations were made over 1717–1723 UT and recorded on Kodak Technical Pan photographic emulsion, then digitized at the National Solar Observatory, Sac Peak, to 4000 × 4000 pixels, each 0.58 arcsec square. Recovered data from the rocket flight consists of exposures ranging from 10 to 60 seconds in duration. Some of the images, notably the 60-second exposure, have scratches due to high-velocity impact of the rocket with the desert floor. For the present analysis, one 60-second and one 30-second exposure were used.

We define an XBP as a compact, isolated x-ray structure. We make no *a priori* assumptions about size range or associated magnetic structure. We are particularly concerned about including two types of points in our study: XBPs that fall outside the traditional 10–30" range, and XBPs that have underlying bipolar magnetic fields. Since the latter points are so common, we shall call them *bipolar* XBPs.

To find the XBPs from 12 April 1993, we examine the 60-second exposure, taken starting at 1718 UT, and a 30-second exposure taken at 1721 UT. Both are shown in Figure 1. Using the 60-second image at full resolution, we examine the solar disk in detail, studying only a 500 × 500 pixel area, corresponding to 290 × 290 arc-seconds, at any one time. This allows us to distinguish features with respect to the local background, rather than the full disk background. Our XBP candidates are any compact, isolated x-ray structures noticeably brighter than the local background. (We say "candidate" because some apparent XBPs may turn out to be other identifiable structures, such as x-ray loop footpoints.) When an XBP candidate is found, we compare that region to the same area on the aligned 30-second exposure. If the feature appears on both images, we assume it is a genuine x-ray feature (as opposed to a chance exposure of the film due to an emulsion defect or other non-solar source).

In order to determine the underlying magnetic structure of our XBP candidates, we compare them with near-contemporaneous Big Bear Solar Observatory and Kitt Peak National Observatory magnetograms. (The magnetogram times range from 1739 to 1806 UT, very close to the NIXT flight time.) *A priori*, we

expect to find many bipoles, some indeterminate magnetic structures, and some monopoles (i.e. structures whose opposite polarity component is not detected). All are perfectly acceptable bright points except for unipolar structures that are clearly part of a larger loop; we wish to exclude such footpoints from consideration, since they fail to satisfy the criteria that XBPs must be compact and isolated.

We expect that XBPs with clear magnetic association will be concentrated toward the center of the disk due to line-of-sight effects in the magnetogram. (The magnetogram measures the line-of-sight component of the magnetic field, which decreases as $\cos\theta$, where $\theta$ is the angle relative to the line of sight.) Because of this effect, when drawing conclusions about the number of XBPs with a given type of magnetic signature we will need to restrict attention to those XBPs in a central region of the disk, away from the limb.

## 3. Observational Results

Using the method for finding XPBs outlined above, we find 172 x-ray bright point candidates, as seen in Figure 2. When compared to the magnetograms, we find that only two of these points are loop footpoints, leaving 170 genuine x-ray bright points. This is the highest level of single disk bright point activity observed to date; previously, the largest number found was 122, observed during a rocket flight on 16 September 1976 near the minimum of solar cycle 21 (Golub, Davis, & Krieger 1979).

Since most theoretical models rely on cancelling magnetic flux, we focus particularly on bipolar XBPs. Our survey finds that 93 XBP candidates show positive bipolar association; Figure 3 shows which bright points have underlying bipoles. For our purposes, "bipolar" is broadly defined; any point with one or more regions of opposite polarity qualifies as bipolar. Often it is difficult to determine which bipole corresponds to which bright point, and in fact the converging flux model predicts that XBPs will not necessarily form directly over their corresponding magnetic bipoles (Parnell, Priest, & Titov 1994).

As expected, these 93 bipolar XBPs are concentrated away from the limb. We suspect that many of the non-bipolar XBPs near the limb actually have corresponding bipoles, which are simply too faint to see due to line-of-sight effects.

To get an estimate for total number of bipolar XBPs, we find the percentage of points that are bipolar in a central region of the disk and then multiply by the total number of XBPs. We determine $0.8R_\odot$ as the boundary for disk center. Beyond this point, $\cos\theta \leq 0.6$, and the magnetogram line-of-sight effects cause most bipoles to be obscured (Figure 3). 83 XBP candidates are observed inside the resulting "inner circle."

Of these 83 points, 71 are bipolar, so approximately 86%, or $71/83 \times 170 = 145$, of the observed XBPs are expected to have bipolar signatures. This calculation ignores the possibility that the frequency of bipolar XBPs varies as a function of latitude; since the $0.8R_\odot$ circle preferentially eliminates high-latitude points, any such variation is likewise excluded from consideration.

Examples of bipolar XBPs, chosen from the inner circle, show much morphological diversity (Figure 4). In examining details of the associated magnetic structures, we find that most of them are simple bipoles. Figures 4a–4e show examples of this basic bipolar structure. However, 16 of the 93 observed magnetic structures are more complicated. Most of these configurations possess a single point of one polarity connected to multiple points of the opposite polarity (Figures 4i and 4j), and some XBPs correspond to multiple bipoles (Figures 4g and 4h). There is even an example of both of these effects simultaneously (Figure 4f). Such multipolar structures remind us that a simple bipolar model for XBPs is an idealization; there are many XBPs with more intricate magnetic structure.

## 4. Analysis and Discussion of Results

Having observed 170 x-ray bright points (with 93 of them definitely bipolar), we have a source for a statistically significant analysis of various XBP properties. From this data set, we examine XBP latitude distributions, size, and emitted magnetic flux.[*** ¡– WHAT DOES THIS MEAN?? ***].

### 4.1. Latitude Distribution

We calculate latitude density distribution as a function of quiet sun disk area. Since active regions would obscure any bright points forming in the same area, we subtract off active region areas from the total disk area. Of course, the effective area of a given patch of the sun increases as we move toward the limb; when calculating number densities, we take this variation into account. The resulting density distributions appear in Figures 5–8.

The figures show that there are no systematic trends in bright point distribution, either by absolute latitude or by hemisphere. (The sharp downward trend *** ... [WHERE? TOWARD THE LIMB? TOWARD THE POLES?] ... *** for bipolar XBPs is almost certainly due to the line-of-sight effects discussed above.) Such a lack of correlation may be consistent with the Harvey & Strong observations [REFERENCE].

**** [PLEASE ADD SOME WORDS ABOVE. FOR INSTANCE, DOES 'no systematic trends'
MEAN A UNIFORM COSINE DISTRIBUTION? ] *****

## 4.2. Size Range

Our primary measure of XBP size is area; since XBPs vary widely in shape, a single dimension is
insufficient to characterize their size completely. Nevertheless, since XBP sizes are traditionally given by
characteristic lengths, we also calculate the "diameters" of the XBPs; we define the diameter of an XBP as
the longest chord that fits inside the XBP.

A distribution of the resulting XBP sizes appears in Figure 9; we plot histograms for both the total
XBP sample and for magnetically correlated bright points. The observed range of sizes is larger than
the commonly assumed 10–30", although the majority of the bright points are smaller than 20". Both
distributions have a mode at ~12", and the shape of the two curves is similar. The number of XBPs
larger than the mode tapers off to a maximum of 40", while the XBPs smaller than the mode are more
concentrated. The smallest bright point that we observe is 3", or 5 pixels, across. Such a point is close to
the lower limits of our resolution, and the shape of the graph suggests that smaller XBPs may exist.

## 4.3. Energy Calibration

For analysis purposes, the NIXT flight film (Kodak Tech Pan) was enlarged and then digitized using a
micro-densitometer at SAC Peak. After digitization, each image consists of $4000^2$ pixels. An X-ray intensity
calibration was obtained by exposing film with the same emulsion as the flight film to a 67.6 Å source
(Spiller, et al.1991). The calibration film and flight film underwent identical development, enlargement and
digitization procedures. However, because the base plus fog levels of the flight film differed from those of
the calibration strips, a simple transformation must be applied to the calibration strip data before it will
yield a calibration for the flight film.

An independent calibration of the relative X-ray exposure can be obtained from the flight film itself,
because there is no reciprocity failure for the film when it is exposed to X-rays. We use a bootstrap
method as follows: after precision alignment of the images, we found all the points on say, a 30 second
image, which were located at positions where the densitometer units were a specified value on a 60 second
image. The average value of the densitometer units on the 30 second image at these locations then gives

a two point energy calibration, since the ratio of the X-ray exposures is known to be the inverse of the exposure time ratio. In other words, the specified densitometer value for the 60 second image corresponds to twice the exposure of the average value obtained from the 30 second image. Note that the distribution of densitometer values on the 30 second image at these locations yields estimate of the precision of individual densitometer values. The distributions were typically characterized by a FWHM of 200 to 300 densitometer units.

By appropriately choosing the specified densitometer unit values and repeating the process, this method can be used by itself to obtain a complete relative energy calibration. For example, pick the first specified densitometer value for the 60 second image (call it $D_1$) to be the value of the most exposed regions, and, as above, obtain an average value from the same locations on the 30 second image (call it $D_2$). Then, use $D_2$ as the next specified value for the 60 second image, finding a new set of locations and a new average densitometer value for these locations on the 30 second image (call this new value $D_3$). This process can be repeated until $D_n = D_{n+1}$, at which point the base plus fog level has been reached and further iterations are pointless. We then have a set of densitometer values, $\{D_1, D_2, D_3, D_4, \ldots\}$, and a corresponding set of relative X-ray exposures, $\{1, \frac{1}{2}, \frac{1}{4}, \frac{1}{8}, \ldots\}$, which we will refer to as a bootstrap. The calibration curve in figure 10 was derived from bootstrap method. These curves are identical to H-D curve, aside from the vertical scale, because the densitometer unit values are directly proportional to the photographic density of the enlarged film.

The errors in this bootstrap method are estimated by obtaining bootstraps using different image pairs, and with different starting points. All the points from 27 bootstraps using the April flight film are shown in figure 10 . Some bootstraps were obtained from a 60 second, 30 second image pair, and some were obtained from a 30 second, 10 second image pair. The various bootstraps follow each other well over the linear portion of the H-D curves, which are characterized by a straight line whose slope equals the contrast index of the film. However, the extrapolation down into the base plus fog region of the curves is less certain, with base plus fog levels varying by as much as a few hundred densitometer units, depending on the bootstrap.

To set the absolute X-ray exposure scale for the bootstrap calibrations, we used the calibration strip data. The two different types of calibration also serve as a valuable cross check on each other. The relationship between samples of the same film with different base plus fog levels is adequately described by the linear relationship $D_A = \alpha D_B + \beta$, where $D_A$ and $D_B$ are the photographic densities of the two film samples (Simon, et al.197?). Thus, to determine the absolute scale of the bootstrap calibrations, we

used a three parameter fit of the calibration strip data to the bootstraps. The three parameters were the two constants mentioned above, $\alpha$ and $\beta$, and a multiplicative constant to set the X-ray exposure scale. These were found by minimizing $\chi^2$. The overall uncertainty in the exposure scale, as determined by the deviations in parameter space required to raise $\chi^2$ by 1 above its minimum value, is about a factor of two. The calibrations and modified calibration strip data are shown in figure 10 .

## 4.4.  Emitted Energy Flux

To determine the flux per bright point, we isolate each point into two rectangular regions–one immediately enclosing the XBP, and a larger rectangle enclosing both the bright point and a portion of the local background. The central rectangle is then subtracted out of the larger rectangle, and the remaining area is considered the local background. Two sets of histograms are made: one of the XBP emitted energy flux, and the other of emitted energy flux of the local background. This method is used on both the 30- and the 60-second exposures. The corresponding histograms from the 30- and the 60-second images are summed, and we take the mode of the result as the emitted energy flux value for the region. Figures 11 and 12 show examples of these histograms for the XBPs from Figure 4.

We define the bright point flux as the total flux measured for the XBP minus the flux of the local background. In order to eliminate possible systematic effects due to variations in the local background flux, we also consider, as a separate data set, XBPs drawn from the coronal hole regions at the poles and to the east of the active region. Since coronal holes are characterized by extremely dim local background, we can assume that XBPs observed in these regions are the least likely to be influenced by systematic effects due to background subtraction. A distribution of emitted x-ray flux per unit area is shown in Figure 13. The figure includes flux emission from all three data sets. Note that most bright points emit between 0.04 and 0.40 milliergs/cm$^2$/sec, with scattered XBPs emitting much more; the outliers are mostly flaring XBPs. The XBPs in the coronal holes tend to have lower emitted flux. —¿ *** !!! [BAD NEWS!! THIS IMPLIES THAT THE SUBTRACTION IN THE OTHER AREAS HAS NOT BEEN DONE CORRECTLY!!] !!! ***

We examine the total energy flux as a function of size (Figures 14–16). Surprisingly, we find no correlation between flux and size. In fact, with the exception of the flaring XBPs, most of the energy flux falls into a well-defined band. Figure 16, which shows the correlation of bright points in coronal holes, should give us the best understanding of correlation, as the XBPs will be subject to the least amount of influence from local background. But even here we see no correlation. If anything, the energy flux range is

actually better defined.

## 5. Conclusion

Results of this study offer us greater clarification as to the characteristics of the x-ray bright point. We find that XBPs range in size from $\leq$ 3-40", rather than the narrower, more commonly used 10-30", and our minimum may be due to resolution limitations, rather than a phenomenological size cutoff. We also observe that bright points are generally associated with bipolar magnetic structures, although not necessarily simple bipoles. The significant fraction of complex structure observed leads us to believe that enhanced resolution may show intricate loop systems even at the smallest scales. In examining XBP luminosity, we find that emitted x-ray flux is confined to a narrow range of 0.04-0.4milliergs/cm$^2$/sec. Surprisingly, this measurement shows no correlation with size. While not conclusive, it is possible that this limited flux range is itself characteristic of x-ray bright points.

Our results call for more in-depth research on the structures and mechanisms of x-ray bright points. In spite of excellent resolution and a large single-disk sample, our study suffers from one major limitation. By using data collected during a sounding rocket flight, our observations only offer a few minutes of time resolution, making the study of dynamics extremely difficult. While continuous data is available from the *Yohkoh* SXT and now SoHO/EIT, neither of these instruments offers spatial resolution comparable to NIXT (both *Yohkoh* and EIT have $\sim$ 2.5" pixels). With the majority of our XBPs measuring less than 20", sub-arc-second resolution would seem essential for any complete study of bright point morphology and dynamics.

The expected launch of TRACE in December 1997 will offer the opportunity to observe the corona continuously at sub-arc-second resolution ($\sim$ 0.5" pixels). In overcoming current spatial and temporal limits, TRACE will make it possible to examine bright points in more depth. Previously, XBP studies have tended to focus on phenomenological statistics. With TRACE, the questions of structure and mechanisms can be more thoroughly addressed. Since x-ray bright points exist at the limits of our current resolution, it has been difficult to examine all but the simplest structure. Data from TRACE will allow us to determine the extent to which XBPs are morphologically complex. Comparisons between TRACE and SoHO/MDI magnetograms will also offer insight into the connections between XBPs and the magnetic network. Such contemporaneous data will enable us to verify the converging flux model (Priest, Parnell, & Martin 1994), as well as examine the question of the often observed misalignments between bright points and their

corresponding bipoles (Kankelborg, et al. 1996). There is also hope that, since TRACE functions in a temperature range similar to NIXT, the narrow energy flux range we observe can be studied and an explanation can be offered.

As instruments like TRACE (0.5" pixels), Solar-B (1" pixels), and HIREX (0.01" pixels) become available, the study of small coronal phenomena, such as x-ray bright points, stands to improve drastically. Detailed observations of the tiniest structures may not only provide explanations for existing questions, but will almost certainly raise new ones. We stand on the threshold of a facet of solar physics, one is which the Sun can be examined and understood on a microscopic level.

Fig. 1.— NIXT photographs. Left: 30-second exposure. Right: 60-second exposure.
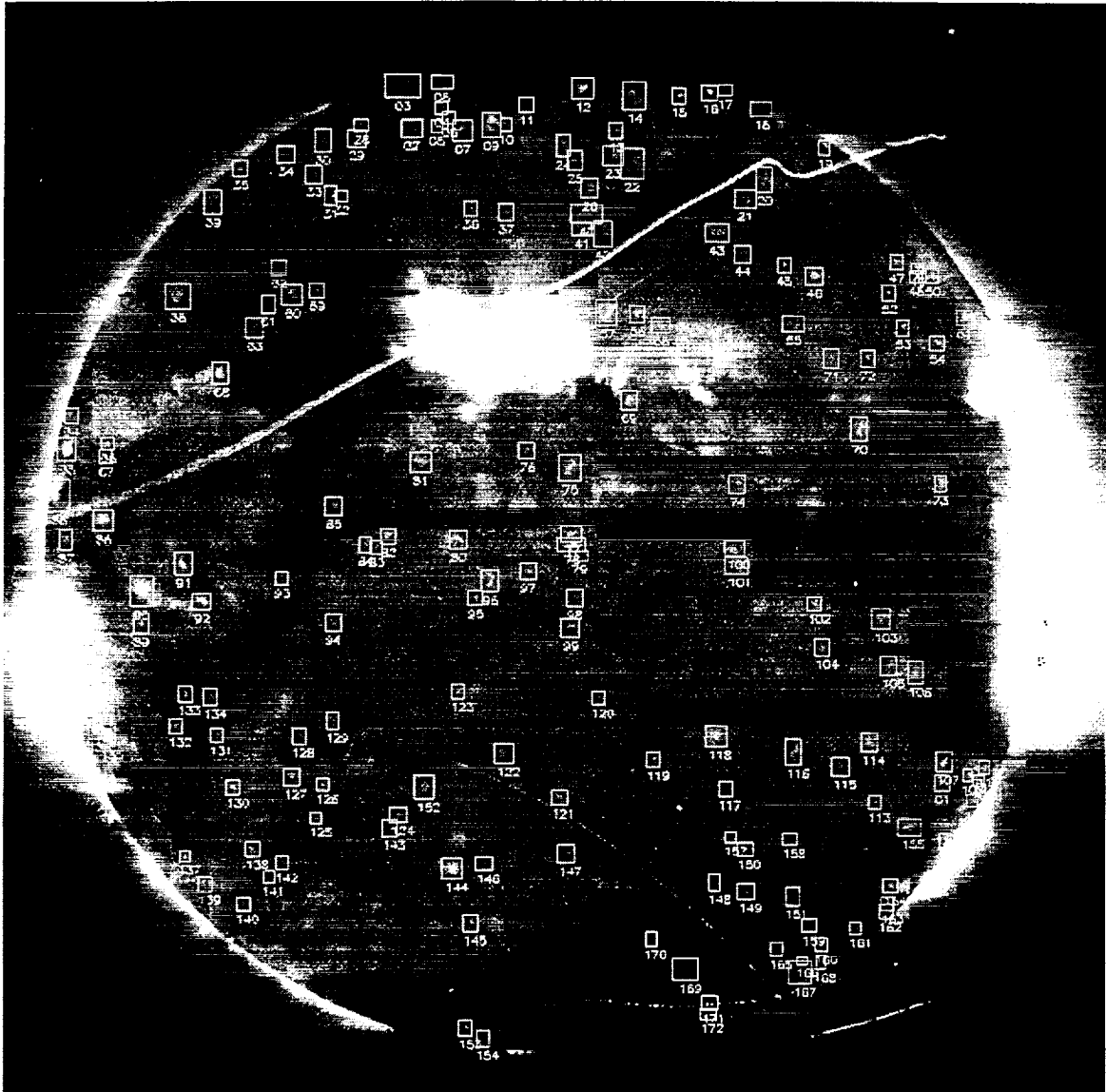
Fig. 2.— NIXT full-disk image with XBPs.
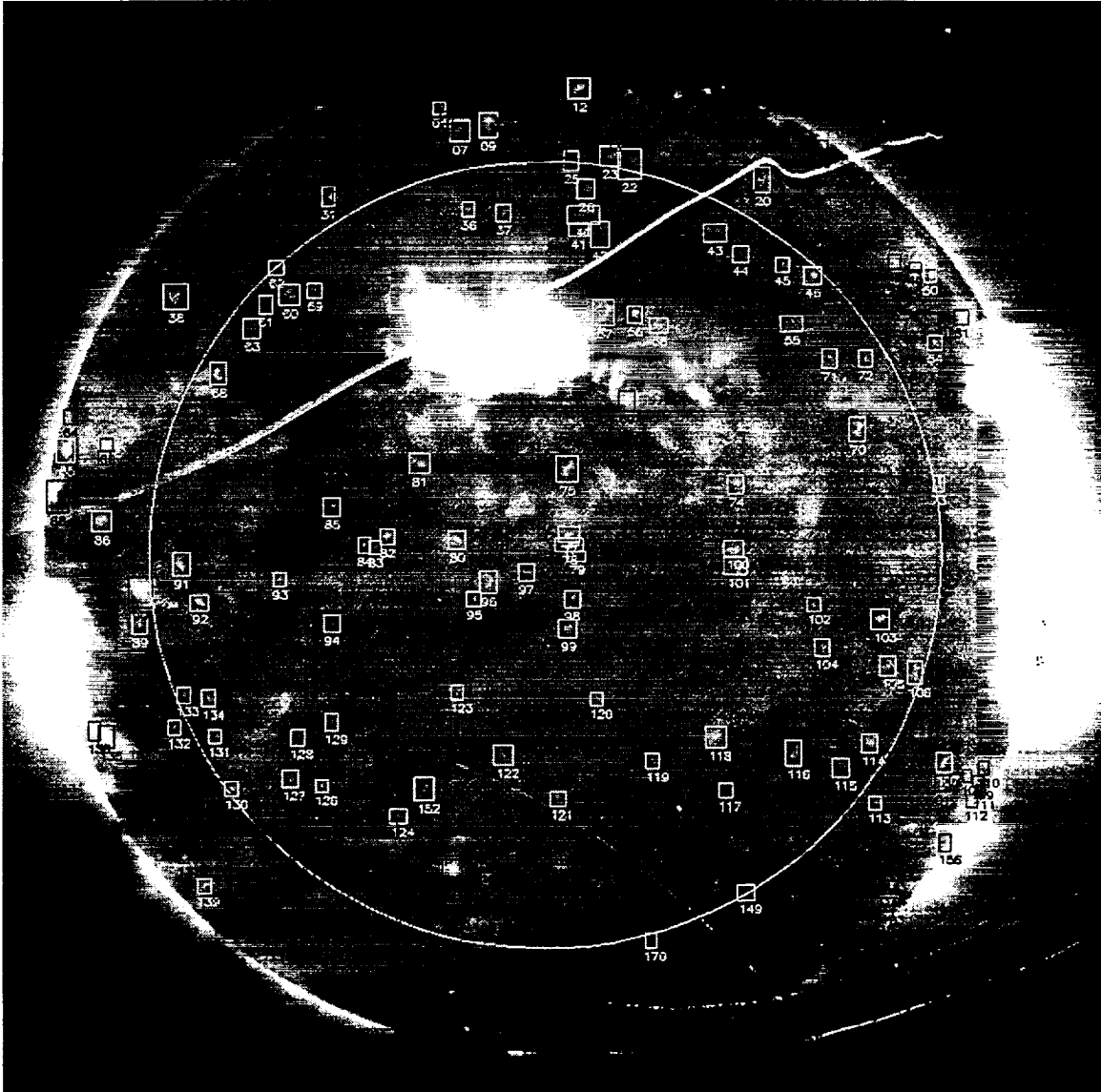
Fig. 3.— NIXT full-disk image with XBPs. XBPs with bipolar magnetic structure are white, while the others are black. The circle has radius $0.8R_\odot$; outside this circle VMG line-of-sight effects decrease our ability to find magnetic correspondence.
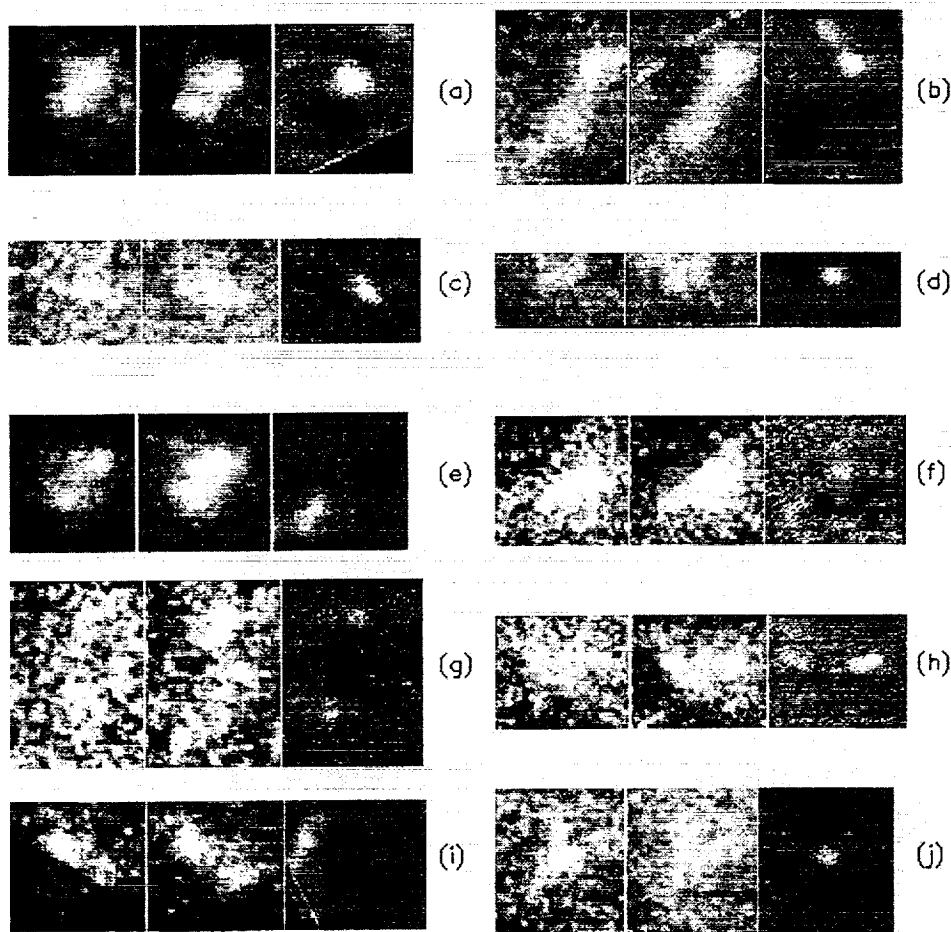
Fig. 4.— The XBPs shown here correspond to the following labels in the previous figure: (a)–56, (b)–57, (c)–58, (d)–79, (e)–82, (f)–23, (g)–42, (h)–43, (i)–81, (j)–115. Images (a)–(e) are examples of the most common type of x-ray bright points, which are associated with simple bipolar structure. (g)–(h) show bright points corresponding to multiple bipolar structures. In (i)–(j), we can see x-ray bright points associated with structures containing a single pole of one polarity and multiple poles of the opposite polarity. Image (f) shows a combination of several of these features.
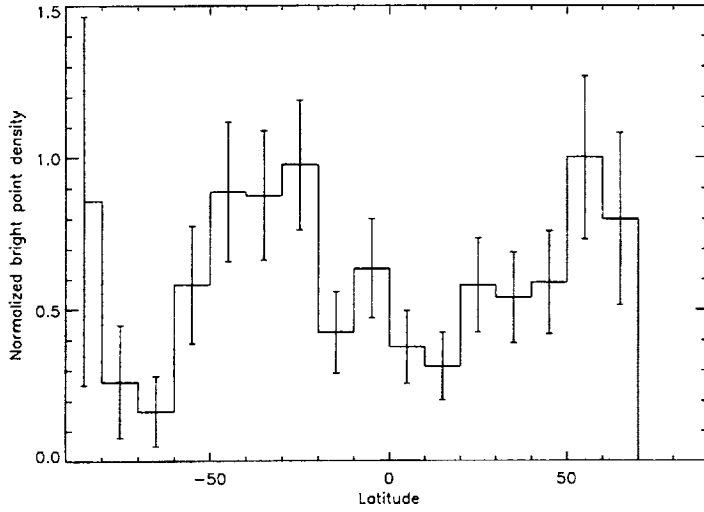
Fig. 5.— Density distribution as a function of latitude for all XBPs.
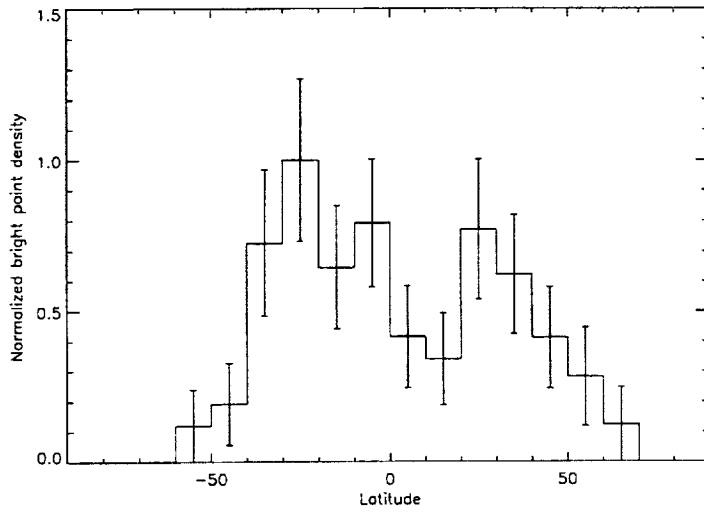


Fig. 6.— Density distribution as a function of latitude for XBPs with an identifiable magnetic character.
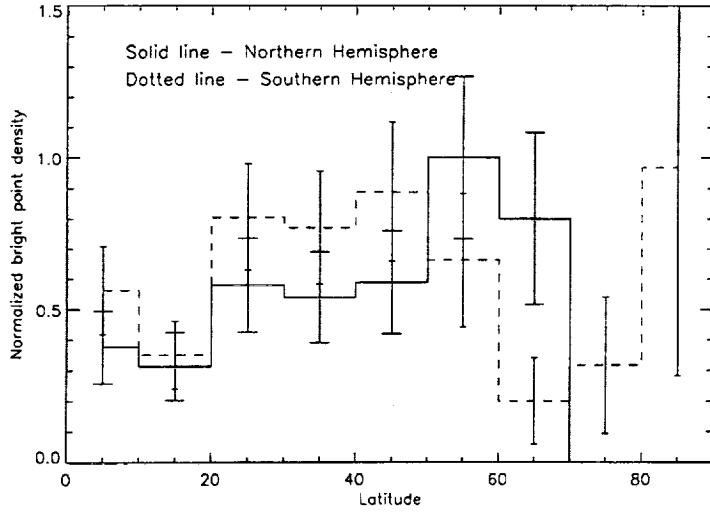
Fig. 7.— Comparison of north and south latitude distributions for all XBPs.
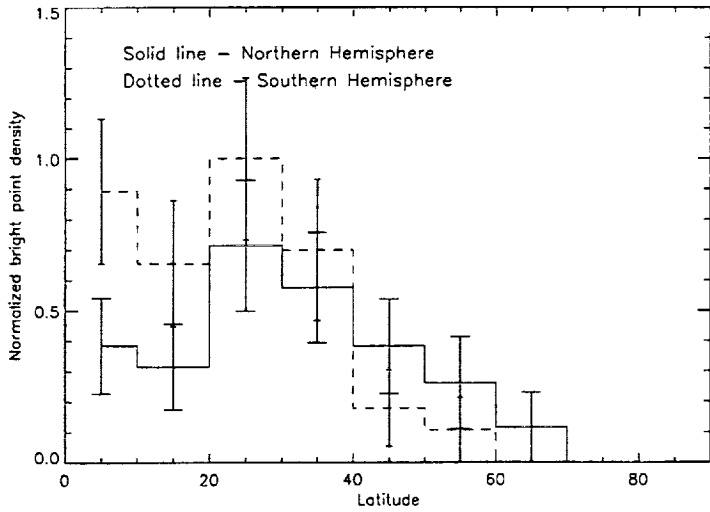


Fig. 8.— Comparison of north and south latitude distributions for XBPs with an identifiable magnetic character.
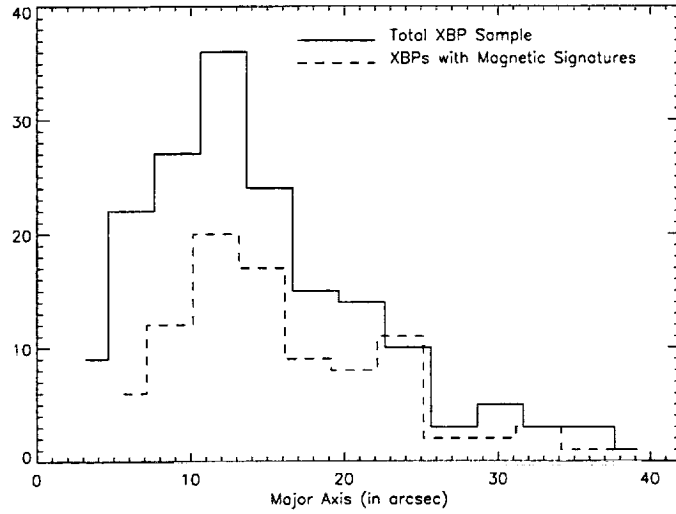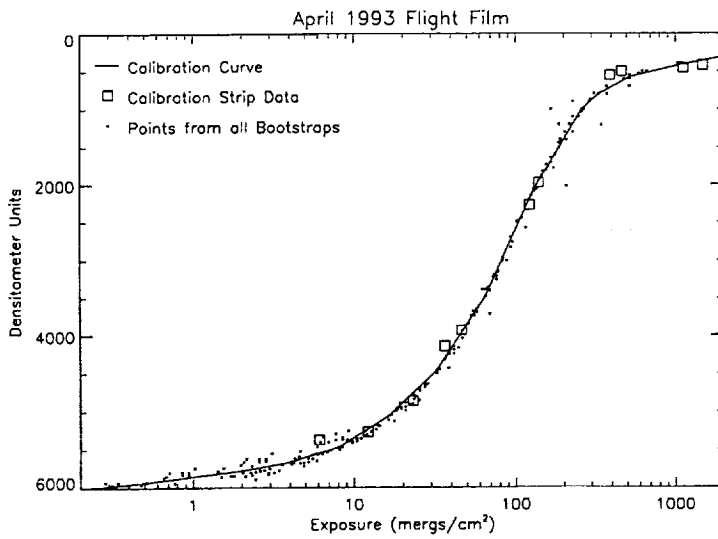
Fig. 9.— Histogram of XBP size distribution.



Fig. 10.— The X-ray energy calibrations for all four sets of flight film. The curves are derived from the 'bootstrap' method described in the text, with the exposure scale being set by the calibration strip data.
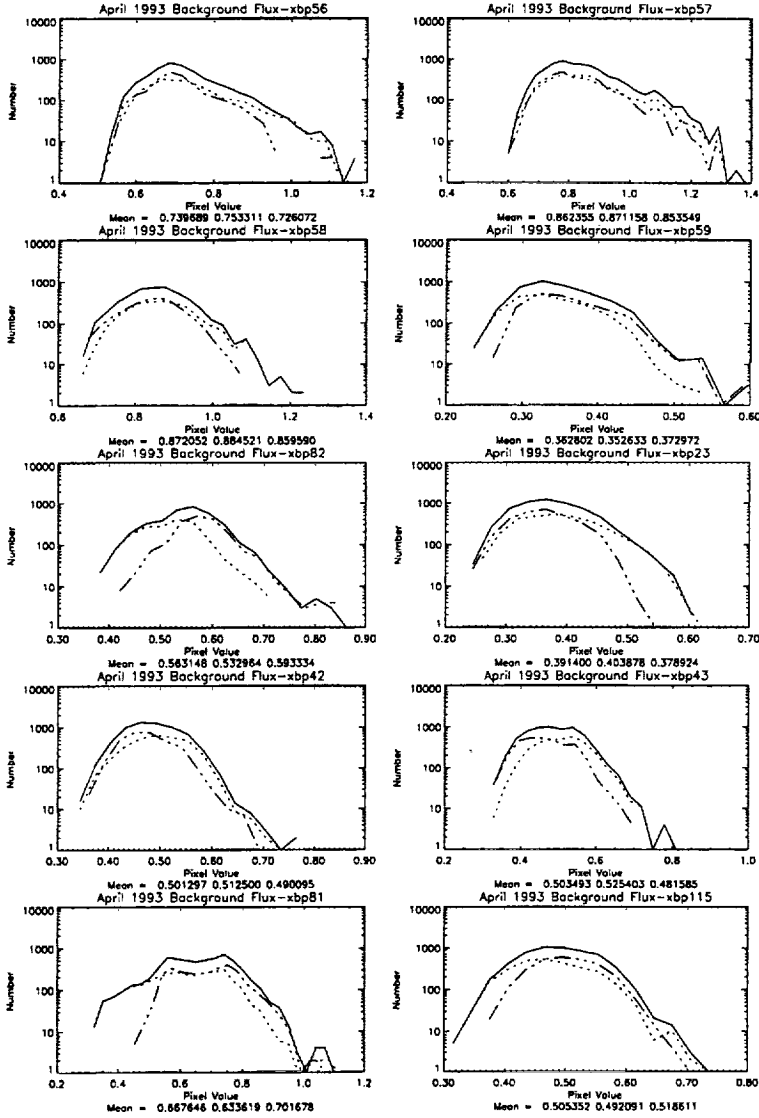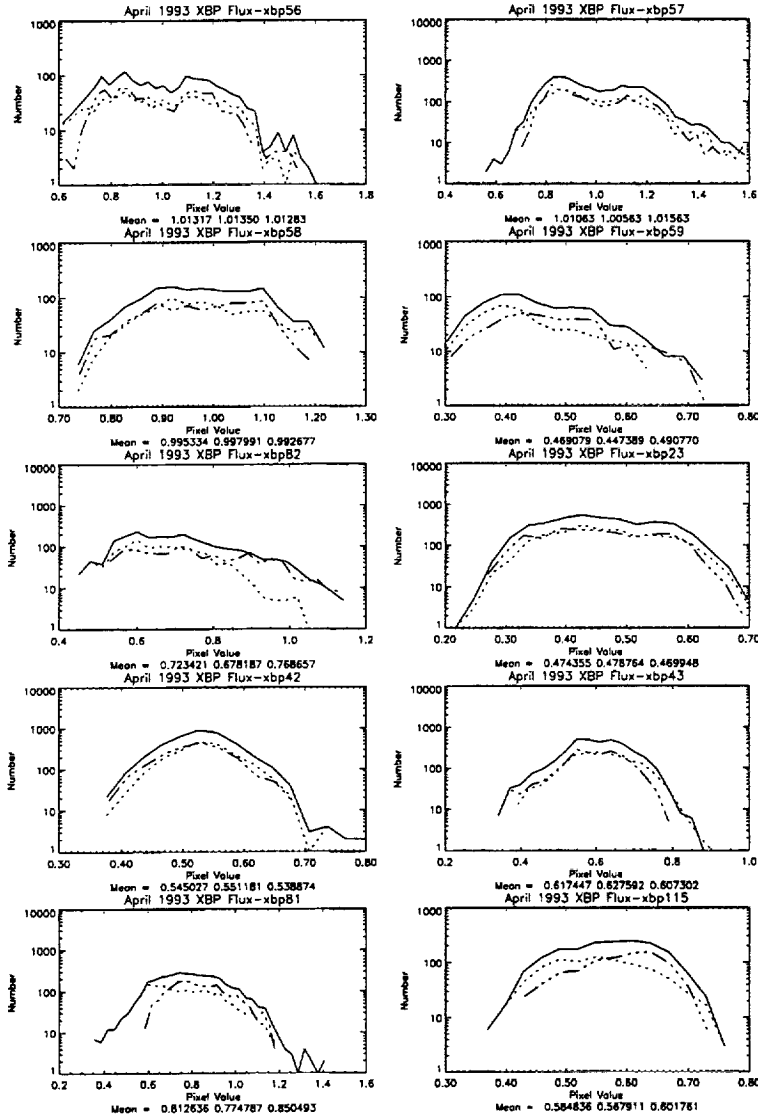
Fig. 11.— Histograms for the bright point background x-ray flux for each of the examples used in Figure 4. The dotted line corresponds to the 60-second exposure, the dashed line corresponds to the thirty-second exposure, and the solid line is the sum of the two. The mode of the solid line is taken as the total background x-ray flux. This number is subtracted from the total flux in order to determine the average x-ray flux per XBP.

Fig. 12.— Histograms for the bright point emitted x-ray flux for each of the examples used in Figure 4. The dotted line corresponds to the 60-second exposure, the dashed line corresponds to the thirty-second exposure, and the solid line is the sum of the two. The mode of the solid line is taken as the total emitted x-ray flux. From this, the background flux is subtracted in order to determine the average x-ray flux per XBP.
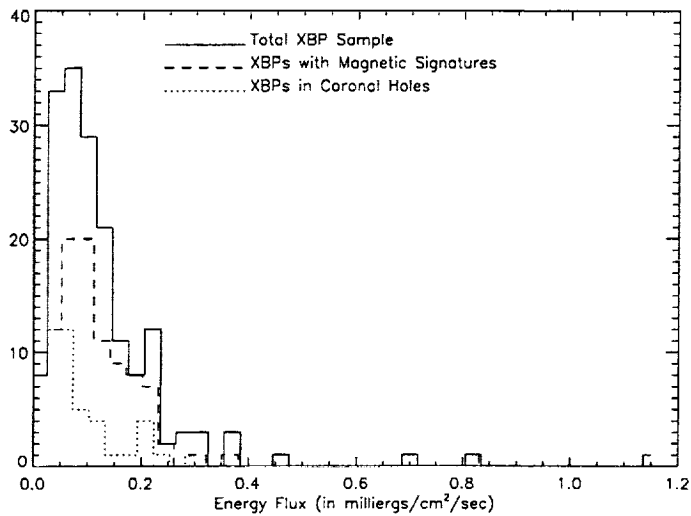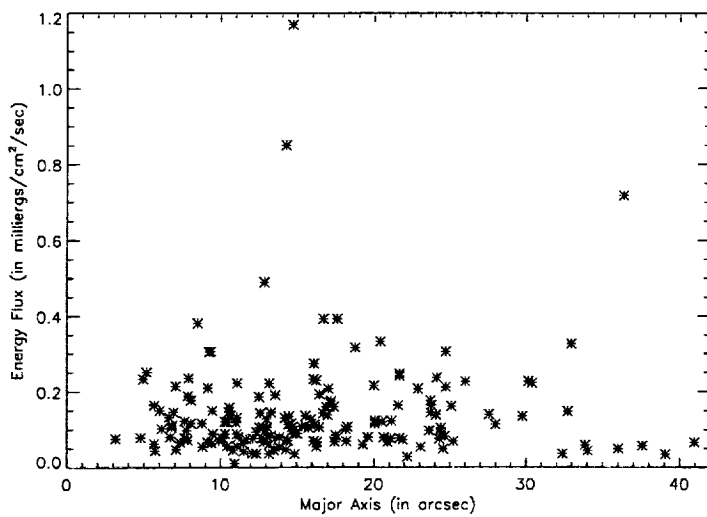
Fig. 13.— Histogram of XBP energy flux.


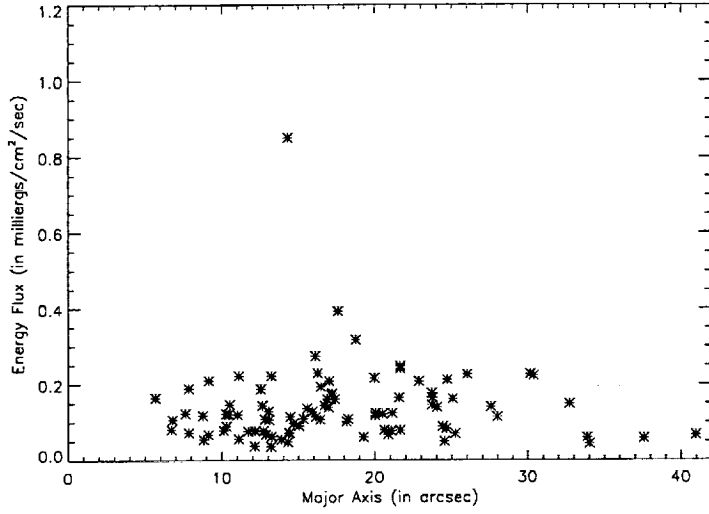
Fig. 14.— Size vs. flux for entire XBP sample.
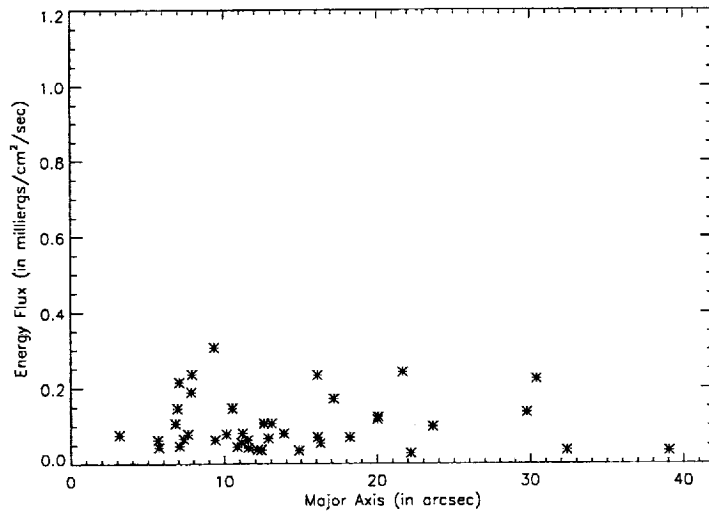
Fig. 15.— Size vs. flux for bipolar XBPs.



Fig. 16.— Size vs. flux for XBPs in coronal holes.

# REFERENCES

Golub, L. 1980, Phil. Trans., R. Soc. A, 297, 595

Golub, L., Davis, J. M., & Krieger, A. S. 1979, ApJ, 229, L145

Golub, L., Harvey, K., & Webb, D. 1986, Goddard Spaceflight Center Coronal and Prominence Plasmas, 365

Golub, L., Krieger, A.S., Silk, J.K., Timothy, A.F. and Vaiana, G.S. 1974 ApJ, 189, L93

Golub, L., Nystrom, G., Herant, M., Kalata, K., & Lovas, I. 1990 Nature 344, 842

Golub, L., & Pasachoff, J. 1997, The Solar Corona, Cambridge University Press

Golub, L., Zirin, H., & Wang, H. 1994, Solar Phys., 153, 179

Kankelborg, C. C., Walker, A. B. C., Hoover, R. B., Barbee, T. W. 1996 ApJ, 466, 529

Moses, D., Cook, J. W., Bartoe, J. D. F., Brueckner, G. E., Dere, K. P., Webb, D. F., Davis, J. M., Harvey, J. W., Recely, F., Martin, S. F., & Zirin, H. 1994 ApJ, 430, 913

Parnell, C. E., Priest, E. R., & Golub, L. 1994, Solar Phys., 151, 57

Parnell, C. E., Priest, E. R., & Titov, V. S. 1994, Solar Phys., 153, 217

Priest, E. R., Parnell, C. E., & Martin, S. F. 1994, ApJ, 427, 459

Sheeley, N. R., Golub, L. 1979, Solar Phys., 63, 119

Simon, R., Haggerty, R., Golub, L., Krieger, A.S., Silk, J.K., Timothy, A.F., & Vaiana, G.S., 1974, Response of Photographic Film to Soft X-ray Radiation, AS & E.

Spiller, E., McCorkle, R.A., Wilcaynski, J.S., Golub, L., Nystrom, G., Takacs, P.Z., Welch, C., 1991 Optical Eng., 30, 1109.

Strong, K. T., Harvey, K., Hirayama, T., Nitta, N., Shimizu, T., & Tsuneta, S. 1992, PASJ, 44, L161

Tang, F., Harvey, K., Bruner, M., Kent, B., & Antonucci, E. 1982, Advances in Space Research, 11, 65

Webb, D. F., Martin, S. F., Moses, D., & Harvey, J. W. 1993, Solar Phys., 144, 15

Webb, D. F., & Moses, D. 1989, Solar X-Ray Astronomy Sounding Rocket Program, (Cambridge, MA: AS&E)

Webb, D. F., & Moses, D. 1990, Advances in Space Research, 10, 185